University of Groningen

ALMA Lensing Cluster Survey

Fujimoto, Seiji; Oguri, Masamune; Brammer, Gabriel; Yoshimura, Yuki; Laporte, Nicolas; Gonzalez-Lopez, Jorge; Caminha, Gabriel B.; Kohno, Kotaro; Zitrin, Adi; Richard, Johan

IMPORTANT NOTE: You are advised to consult the publisher's version (publisher's PDF) if you wish to cite from it. Please check the document version below.

Document Version
Publisher's PDF, also known as Version of record

[Link to publication in University of Groningen/UMCG research database](#)

CrossMark

ALMA Lensing Cluster Survey:
Bright [C II] 158 μm Lines from a Multiply Imaged Sub-$L^\star$ Galaxy at $z = 6.0719$

Seiji Fujimoto[1,2] , Masamune Oguri[3,4,5] , Gabriel Brammer[1,2] , Yuki Yoshimura[6,7] , Nicolas Laporte[8,9] ,
Jorge González-López[10,11] , Gabriel B. Caminha[12] , Kotaro Kohno[7,13] , Adi Zitrin[14] , Johan Richard[15] , Masami Ouchi[5,16,17] ,
Franz E. Bauer[18,19] , Ian Smail[20] , Bunyo Hatsukade[7] , Yoshiaki Ono[17] , Vasily Kokorev[1,2] , Hideki Umehata[7,21] ,
Daniel Schaerer[22,23] , Kirsten Knudsen[24] , Fengwu Sun[25] , Georgios Magdis[1,2,26] , Francesco Valentino[1,2] , Yiping Ao[27] ,
Sune Toft[1,2] , Miroslava Dessauges-Zavadsky[22] , Kazuhiro Shimasaku[3,6] , Karina Caputi[1,28] , Haruka Kusakabe[22] ,
Kana Morokuma-Matsui[7] , Kikuchihara Shotaro[6,17] , Eiichi Egami[25] , Minju M. Lee[29] , Timothy Rawle[30] , and
Daniel Espada[31]
[1] Cosmic Dawn Center (DAWN), Jagtvej 128, DK-2200 Copenhagen N, Denmark; fujimoto@nbi.ku.dk
[2] Niels Bohr Institute, University of Copenhagen, Lyngbyvej 2, DK-2100 Copenhagen Ø, Denmark
[3] Research Center for the Early Universe, Graduate School of Science, The University of Tokyo, 7-3-1 Hongo, Bunkyo-ku, Tokyo 113-0033, Japan
[4] Department of Physics, The University of Tokyo, 7-3-1 Hongo, Bunkyo-ku, Tokyo 113-0033, Japan
[5] Kavli Institute for the Physics and Mathematics of the Universe (WPI), The University of Tokyo, 5-1-5 Kashiwanoha, Kashiwa-shi, Chiba, 277-8583, Japan
[6] Department of Astronomy, Graduate School of Science, The University of Tokyo, 7-3-1 Hongo, Bunkyo-ku, Tokyo 113-0033, Japan
[7] Institute of Astronomy, Graduate School of Science, The University of Tokyo, 2-21-1 Osawa, Mitaka, Tokyo 181-0015, Japan
[8] Kavli Institute for Cosmology, University of Cambridge, Madingley Road, Cambridge CB3 0HA, UK
[9] Cavendish Laboratory, University of Cambridge, 19 JJ Thomson Avenue, Cambridge CB3 0HE, UK
[10] Núcleo de Astronomía de la Facultad de Ingeniería y Ciencias, Universidad Diego Portales, Av. Ejército Libertador 441, Santiago, Chile
[11] Las Campanas Observatory, Carnegie Institution of Washington, Casilla 601, La Serena, Chile
[12] Kapteyn Astronomical Institute, University of Groningen, Postbus 800, 9700 AV Groningen, The Netherlands
[13] Research Center for the Early Universe, School of Science, The University of Tokyo, 7-3-1 Hongo, Bunkyo-ku, Tokyo 113-0033, Japan
[14] Physics Department, Ben-Gurion University of the Negev, P.O. Box 653, Be'er-sheva 8410501, Israel
[15] Univ Lyon, Univ Lyon1, Ens de Lyon, CNRS, Centre de Recherche Astrophysique de Lyon UMR5574, F-69230, Saint-Genis-Laval, France
[16] National Astronomical Observatory of Japan, 2-21-1 Osawa, Mitaka, Tokyo 181-8588, Japan
[17] Institute for Cosmic Ray Research, The University of Tokyo, 5-1-5 Kashiwanoha, Kashiwa, Chiba 277-8582, Japan
[18] Instituto de Astrofisica, Facultad de Fisica, Pontificia Universidad Catolica de Chile Av. Vicuna Mackenna 4860, 782-0436 Macul, Santiago, Chile
[19] Millennium Institute of Astrophysics (MAS), Nuncio Monsenor Santero Sanz 100, Providencia, Santiago, Chile
[20] Centre for Extragalactic Astronomy, Department of Physics, Durham University, South Road, Durham DH1 3LE, UK
[21] RIKEN Cluster for Pioneering Research, 2-1 Hirosawa, Wako, Saitama 351-0198, Japan
[22] Observatoire de Genève, Université de Genève, 51 Ch. des Maillettes, 1290 Versoix, Switzerland
[23] CNRS, IRAP, 14 Avenue E. Belin, F-31400 Toulouse, France
[24] Department of Space, Earth and Environment, Chalmers University of Technology, Onsala Space Observatory, SE-43992 Onsala, Sweden
[25] Steward Observatory, University of Arizona, 933 N. Cherry Ave, Tucson, AZ 85721, USA
[26] DTU-Space, Technical University of Denmark, Elektrovej 327, DK-2800 Kgs. Lyngby, Denmark
[27] Purple Mountain Observatory and Key Laboratory for Radio Astronomy, Chinese Academy of Sciences, Nanjing, People's Republic of China
[28] Kapteyn Astronomical Institute, University of Groningen, P.O. Box 800, 9700AV Groningen, The Netherlands
[29] Max-Planck-Institut f ur Extraterrestrische Physik (MPE), Giessenbachstr., D-85748, Garching, Germany
[30] European Space Agency (ESA), ESA Office, Space Telescope Science Institute, 3700 San Martin Drive, Baltimore, MD 21218, USA
[31] SKA Organisation, Lower Withington, Macclesfield, Cheshire SK11 9DL, UK

Abstract

We present bright [C II] 158 μm line detections from a strongly magnified and multiply imaged ($\mu \sim 20$–160) sub–$L^\star$ ($M_{UV} = -19.75^{+0.55}_{-0.44}$) Lyman-break galaxy (LBG) at $z = 6.0719 \pm 0.0004$, drawn from the ALMA Lensing Cluster Survey (ALCS). Emission lines are identified at 268.7 GHz at $\geqslant 8\sigma$ exactly at the positions of two multiple images of the LBG, behind the massive galaxy cluster RXCJ0600−2007. Our lens models, updated with the latest spectroscopy from VLT/MUSE, indicate that a sub region of the LBG crosses the caustic, and is lensed into a long ($\sim 6''$) arc with a local magnification of $\mu \sim 160$, for which the [C II] line is also significantly detected. The source plane reconstruction resolves the interstellar medium (ISM) structure, showing that the [C II] line is co-spatial with the rest-frame UV continuum at a scale of ~ 300 pc. The [C II] line properties suggest that the LBG is a rotation-dominated system, whose velocity gradient explains a slight difference in redshifts between the whole LBG and its sub-region. The star formation rate (SFR)–$L_{[CII]}$ relations, for whole and sub-regions of the LBG, are consistent with those of local galaxies. We evaluate the lower limit of the faint-end of the [C II] luminosity function at $z = 6$, finding it to be consistent with predictions from semi-analytical models and from the local SFR–$L_{[CII]}$ relation with a SFR function at $z = 6$. These results imply that the local SFR–$L_{[CII]}$ relation is universal for a wide range of scales, including the spatially resolved ISM, the whole region of the galaxy, and the cosmic scale, even in the epoch of reionization.

1. Introduction

Galaxy evolution is regulated by several key mechanisms in the interstellar medium (ISM), such as disk formation, stellar and active galactic nuclei (AGN) feedback, mass building via star formation and galaxy mergers, and clump formations due to disk instabilities. Resolving the ISM structure to study local physical properties in high-redshift galaxies is thus essential in order to understand the initial phase of galaxy formation and evolution.

During recent decades, hundreds of star-forming galaxies at $z > 6$ have been spectroscopically identified, primarily with Lyα lines (e.g., Iye et al. 2006; Vanzella et al. 2011; Pentericci et al. 2011, 2014, 2018; Shibuya et al. 2012, 2018; Ono et al. 2012, 2018; Finkelstein et al. 2013; Oesch et al. 2015, 2016; Stark et al. 2017; Higuchi et al. 2019). The Atacama Large Millimeter/submillimeter Array (ALMA) offers a rest-frame far-infrared (FIR) spectroscopic window for these $z > 6$ galaxies, especially with bright fine-structure lines of [C II] 158 μm and [O III] 88 μm (e.g., Maiolino et al. 2015; Inoue et al. 2016; Pentericci et al. 2016; Knudsen et al. 2016; Matthee et al. 2017, 2019; Carniani et al. 2018; Smit et al. 2018; Bowler et al. 2018; Hashimoto et al. 2018, 2019; Tamura et al. 2019; Fujimoto et al. 2019; Bakx et al. 2020). Since heavy elements produced in stars are returned into the ISM, the metal gas properties traced by these fine-structure lines represent good probes of star formation history and related physical mechanisms (Maiolino & Mannucci 2019). In fact, recent ALMA spatial and kinematic [C II]-line studies have identified signatures of some key mechanisms, including disk rotations (e.g., Jones et al. 2017; Smit et al. 2018), galaxy mergers (e.g., Hashimoto et al. 2019; Le Fèvre et al. 2020), and outflows (e.g., Gallerani et al. 2018; Spilker et al. 2018; Fujimoto et al. 2019, 2020b; Ginolfi et al. 2020). In conjunction with other fine-structure lines of [O III] and [N II], recent ALMA observations also allow us to perform multiple line diagnostics to constrain the dominant ionization state of the ISM gas (e.g., Inoue et al. 2016; Pavesi et al. 2016; Laporte et al. 2019; Novak et al. 2019; Harikane et al. 2020).

There are several challenges associated with FIR spectroscopy. The first is sensitivity. While ALMA is the most sensitive mm/submm telescope, yielding a large number of new findings about high-redshift galaxies, the detection of FIR fine-structure lines from abundant, typical galaxies remains challenging. For example, to observe a [C II] line of $\sim 1 \times 10^8 L_\odot$ from $z = 6$, an observation time of about 2 h is required.[32] However, such a source typically falls in the absolute UV magnitude range of $M_{UV} \sim -22.0 - -21.5$ mag (see e.g., Table 7 in Hashimoto et al. 2019). This absolute UV magnitude range is $\sim$2–3 times brighter than the characteristic luminosity, L^*, in the UV luminosity function at $z > 6$ (e.g., Ono et al. 2018), indicating that $\gtrsim$10 h observation time is necessary to study the abundant, typical galaxies with L^* or sub-L^* luminosities. The second challenge is high spatial resolution observations toward these typical galaxies. Recent Hubble Space Telescope (HST) studies report that the typical effective radius (r_e) in star-forming galaxies at $z > 6$ is estimated to be < 1 kpc ($\simeq 0\rlap{.}''2$) (e.g., Holwerda et al. 2015; Shibuya et al. 2015; Bouwens et al. 2017; Kawamata et al. 2018). The ISM structure most

comparable to the r_e scale could be resolved by ALMA high-resolution observations down to the $0\rlap{.}''02$ scale. However, this requires even longer observation times than the $\gtrsim$10 h estimated above, just for the detection of the typical galaxies. The third challenge is the requirement for prior spectroscopic redshifts due to the narrow frequency coverage of ALMA (7.5 GHz coverage in a single tuning), which may cause potential biases. In most cases, the prior spectroscopic redshift is obtained from Lyα lines. While high-redshift galaxies with Lyα spectroscopic redshifts show weak [C II] lines at a given star formation rate (Carniani et al. 2018; Harikane et al. 2018, 2020; but see Schaerer et al. 2020), a recent study by Smit et al. (2018) indicates that galaxies with no strong Lyα line may emit a strong [C II] line. Since the fraction of Lyα emitters (LAEs; e.g., equivalent width of Ly$\alpha > 25$ Å) is less than 30% among star-forming galaxies with $M_{UV} \sim -21.5$ mag at $z > 6$ (e.g., Stark et al. 2011; Treu et al. 2013; Tilvi et al. 2014; De Barros et al. 2017; Pentericci et al. 2018; Kusakabe et al. 2020), follow-up observations of only those galaxies with secure Lyα lines will systematically miss a majority of the representative population at $z > 6$. An ALMA blind line survey is one possible solution, but novel [C II] line emitters $z > 6$ have not yet been identified, due to the lack of sufficiently deep and large survey volumes (e.g., Matsuda et al. 2015; Aravena et al. 2016; Yamaguchi et al. 2017; Hayatsu et al. 2019; Decarli et al. 2020; Romano et al. 2020; Yan et al. 2020).

In this paper, we report the blind detection of bright [C II] 158 μm lines from strongly lensed multiple images of a sub-L^* galaxy at $z = 6.0719$ behind the massive galaxy cluster RXCJ0600−2007, drawn from the ALMA Lensing Cluster Survey (ALCS). Making full use of large ancillary data sets, including HST, Spitzer, and VLT, and with help of gravitational lensing magnification, we resolve the ISM structures and investigate the spatially resolved rest-frame UV-to-FIR continuum, and the [C II] line properties down to a $\simeq$300 pc scale. This is the first ALMA study to resolve the ISM properties in a representative ($\simeq$sub-L^*) galaxy in the epoch of reionization.

The structure of this paper is as follows: in Section 2, we overview the ALCS survey and the data sets in RXCJ0600−2007, as well as strong lensing mass models of the cluster. Section 3 outlines methods of blind line identification, and the optical–near-infrared (NIR) properties of the two [C II] line emitters at $z = 6.07$. In Section 4, we report and discuss the intrinsic characteristics of these two [C II] line emitters together with the correction of the lensing magnification. A summary of this study is presented in Section 5. Throughout this paper, we assume the Chabrier initial mass function (Chabrier 2003) and a flat universe, where $\Omega_m = 0.3$, $\Omega_\Lambda = 0.7$, $\sigma_8 = 0.8$, and $H_0 = 70$ km s^{-1} Mpc^{-1}. We use magnitudes in the AB system (Oke & Gunn 1983).

2. Data and Reduction

2.1. ALMA Lensing Cluster Survey

ALCS is a cycle-6 ALMA large program (Project ID: 2018.1.00035.L; PI: K. Kohno) to map a total of 88 arcmin^2 high-magnification regions in 33 massive galaxy clusters at 1.2 mm in Band 6. The sample is selected from the best-studied clusters drawn from HST treasury programs, i.e., the Cluster Lensing And Supernova Survey with Hubble (CLASH; Postman et al. 2012), Hubble Frontier Fields (HFF; Lotz et al. 2017), and the Reionization Lensing Cluster Survey

---

[32] Based on CASA Observation Tool calculations to detect the [C II] line of $1 \times 10^8 L_\odot$ with a line width of 200 km s^{-1} at $\geqslant 5\sigma$ in the velocity-integrated map.

(RELICS; Coe et al. 2019). Observations were carried out between 2018 December and 2019 December, in compact array configurations of C43-1 and C43-2, fine-tuned to recover strongly lensed (i.e., spatially elongated), low surface brightness sources. The 1.2 mm mapping is accomplished by means of a 15 GHz wide spectral scan in the ranges of 250.0–257.5 GHz and 265.0–272.5 GHz via two frequency setups, so as to enlarge the survey volume for line-emitting galaxies. The spectral mode of Time Division Mode is used, which achieves a spectral resolution of ~ 28 km s^{-1} with these frequency setups. A full description of the survey and its main objectives will be presented in a separate paper (currently in preparation).

2.2. RXCJ0600−2007

RXCJ0600−2007 is a massive ($\sim 10^{15} M_{\odot}$) galaxy cluster at $z = 0.43$, which is included in RELICS, and was first identified in the Massive Cluster Survey (MACS; Ebeling et al. 2001). As a part of ALCS, the ALMA observations for RXCJ0600−2007 were performed in 2019 January, mapping the central area of $230'' \times 90''$ in 105 pointings with 46–49 12 m antennae, and providing baselines of 15–456 m under a precipitable water vapor (PWV) of 0.6–1.3 mm. J0522-3627 was observed as a flux calibrator. The bandpass and phase calibrations were performed with J0609-1542.

The ALMA data were reduced and calibrated using the Common Astronomy Software Applications package version 5.4.0 (CASA; McMullin et al. 2007) with the pipeline script, in the standard manner. With the CASA task TCLEAN, continuum maps were produced by utilizing all spectral windows. The TCLEAN routines were executed down to the 3σ level. We adopted a pixel scale of $0''15$, and a common spectral channel bin of 30 km s^{-1}. The natural-weighted map achieved a synthesized beam FWHM of $1''22 \times 0''95$, with sensitivities in the continuum and the line in a 30 km s^{-1} width channel of 56.9 and 932 μJy beam^{-1}, respectively. We also produced several uv-tapered maps in a parameter range of $0''8 \times 0''8$ to $1''8 \times 1''8$ to obtain spatially integrated properties where necessary. Throughout the paper, we used the natural-weighted map unless otherwise specified.

HST/ACS–WFC3 and Spitzer/IRAC observations were carried out as a part of the RELICS (Coe et al. 2019) and Spitzer–RELICS (Strait et al. 2020) surveys, respectively. HST images were obtained in the F606W (2180 s), F814W (3565 s), F105W (1411 s), F125W (711 s), F140W (736 s), and F160W (1961 s) filters. The IRAC channel 1 (3.6 μm) and channel 2 (4.5 μm) integrations are approximately 10 hours each. We aligned all of the HST exposures to sources in the PanSTARRS (DR1) catalog (Chambers et al. 2016; Flewelling et al. 2020)—which we verified as consistent with the GAIA DR2 (Gaia Collaboration et al. 2018) astrometric frame—and created final mosaics in a common pixel frame with 50 mas and 100 mas pixels for the ACS/WFC and WFC3/IR filters, respectively. We aligned the individual Spitzer exposures to the same astrometric frame, and generated final drizzled IRAC mosaics with a pixel scale of $0''5$. Further details of the HST (Spitzer) image processing, using `grizli` (`golfir`) software, will be presented in V. Kokorev et al. (2021, in preparation). In Figure 1, we present a false-color HST image of RXCJ0600−2007.

VLT/MUSE integral field spectroscopy of the RXCJ0600−2007 field was obtained on 2018 January 26th (ESO program ID 0100.A-0792, P.I.: A. Edge). The 0.8 h observation was split into three exposures of 970 s each, centered on the brightest cluster galaxy (BCG), and covering 1 arcmin^2 of the cluster core. We use the standard MUSE reduction pipeline version 2.8.1 (Weilbacher et al. 2014) to create the final data cube. In this process, we used the self-calibration method, based on the MUSE Python Data Analysis Framework (Bacon et al. 2016; Piqueras et al. 2017), and implemented in this version of the reduction pipeline. Finally, we applied the Zurich Atmosphere Purge (ZAP, Soto et al. 2016) to remove those sky residuals not completely removed by the MUSE pipeline.

We used the MUSE data cube to build our redshift catalog in two steps, similarly to Caminha et al. (2017, 2019). We first extracted the spectra of all sources detected in the HST imaging, and in a second step, we performed a blind search for faint-line emitters. This procedure allowed us to measure 76 secure redshifts, of which 16 are emissions from galaxies behind the cluster. This redshift catalog was used to identify the cluster members and multiply imaged galaxies used in strong lens mass modeling (see Section 3.3 for more details). In Appendix A, we summarize the full spectroscopic sample from MUSE.

3. Data Analysis

3.1. Line Identification

We conduct a blind line search in the ALMA data cubes, with channel widths of 30 and 60 km s^{-1}. Firstly, we produce three-dimensional signal-to-noise ratio (S/N) cubes by dividing each channel with its standard deviation. Here we use the ALMA data cubes prior to primary beam correction. We then search line candidates in the three-dimensional S/N cube, utilizing the python-based software, DENDROGRAM (Goodman et al. 2009), whose algorithm is similar to CLUMPFIND (Williams et al. 1994). In DENDROGRAM, we obtain an initial candidate catalog of line sources meeting the following criteria: at least 10 pixels and/or channels with a pixel value of $\geqslant 2$ (i.e., S/N $\geqslant 2$). Performing the same procedure in the negative peaks in the S/N cubes, under the assumption that the noise is Gaussian, DENDROGRAM evaluates the reliability of the initial line candidates based on the positive and negative properties of the peak S/N histograms, spatially-integrated pixel values, and channel width. This results in two reliable, bright-line emitters, both at ~ 268.7 GHz. We note that these two lines are also robustly identified via the independent blind line search method of González-López et al. (2017). Based on the morphological, redshift, and gravitational lens properties of the two line emitters obtained, in the detailed analyses in the following subsections (Sections 3.2, 3.3, and 3.4), we refer to these two line emitters as $z6.1/6.2$ ($= z6.1$ and $z6.2$) and $z6.3$ throughout this paper.

In Figure 1, we present the ALMA spectra and the velocity-integrated intensity (i.e., moment 0) maps of $z6.1/6.2$ and $z6.3$. Note that $z6.1/6.2$ shows an elongated morphology with two peaks in the moment 0 map. Although there is a possibility that a combination of the diffuse continuum and noise fluctuation causes multiple peaks (e.g., Hodge et al. 2016), we confirm in Appendix B that the two peaks in $z6.1/6.2$ are not caused by this combination, via a realistic simulation. A single Gaussian fit to $z6.1/6.2$ and $z6.3$ in the line spectra is summarized in Table 1. Although we obtain consistent full-width-at-half-maximum (FWHM) values for the line widths between $z6.1/$
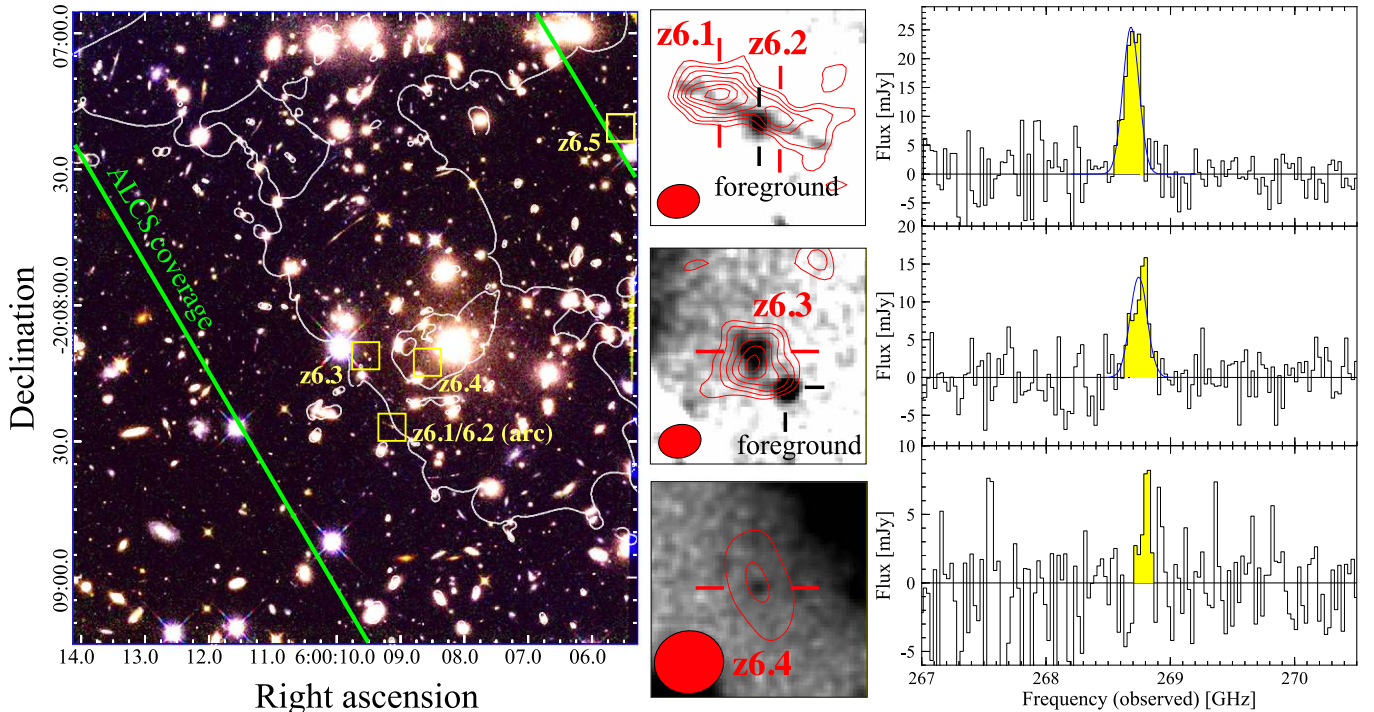
Figure 1. Left: false-color HST image of the cluster RXCJ0600−2007 (red: F160W, green: F125W, blue: F814W). The white line denotes the critical curve at $z = 6.07$, estimated from our fiducial mass model. The green lines indicate the ALCS area coverage in this cluster, within which the relative sensitivity to the deepest part of the mosaic map is greater than 30%. The five multiple image positions of RXCJ0600-$z6$ are marked with yellow $6'' \times 6''$ squares. Middle: HST/F160W $6'' \times 6''$ cutouts for multiple images of $z6.1/6.2$, $z6.3$, and $z6.4$ (from top to bottom). The red contours denote the velocity-integrated [C II] line intensity, drawn at 1σ intervals from $\pm 2\sigma$ to $\pm 8\sigma$. We use the natural-weighted map for $z6.1/6.2$ and $z6.3$, while using the uv-tapered ($1''8 \times 1''8$) map for $z6.4$ to obtain the optimized S/N. The ALMA synthesized beams are presented in the bottom left. The black bars indicate foreground sources. The foreground source overlapping $z6.1/6.2$ is subtracted in our optical–NIR analysis with GALFIT (see Section 3.2 and Appendix C; see also Laporte et al. 2021). Right: [C II] line spectra for $z6.1/6.2$, $z6.3$, and $z6.4$ from top to bottom, obtained from the ALCS data cube. The yellow shade indicates the [C II] integration range for the velocity-integrated map, whose contours are shown in the middle panel. The blue curve is the best-fit single Gaussian.

6.2 and $z6.3$, their frequency peaks differ slightly, by $69 \pm 22 \, \mathrm{km \, s^{-1}}$. Subsequent to integration over a velocity range of $1.5 \times$ FWHM, $z6.1/6.2$ and $z6.3$ have S/N values of 9.2 and 8.0 at the peak pixels, respectively. A single elliptical Gaussian fit over a spatial area of $6'' \times 6''$ in the velocity-integrated maps, using the CASA IMFIT task, yields deconvolved spatial FWHM sizes of $4''24 \times 0''82$, and $1''17 \times 0''29$ for $z6.1/6.2$ and $z6.3$, respectively. To obtain the integrated property, here we use a uv-tapered ($1''0 \times 1''0$) map for $z6.1/6.2$ in IMFIT. From line free channels, the continuum is also detected in the uv-tapered map ($2''0 \times 2''0$) at 4.5σ and 2.5σ level from $z6.1/6.2$ and $z6.3$, respectively. We also summarize the IMFIT results and the continuum flux density in Table 1. Further analyses of the continuum emission are presented in Laporte et al. (2021).

3.2. Optical–NIR Counterparts

The bright lines of $z6.1/6.2$ and $z6.3$ at ~268.7 GHz could be CO or [C II] (e.g., Decarli et al. 2020). To determine which line corresponds to $z6.1/6.2$ and $z6.3$, we investigate their optical to near-infrared (NIR) properties. In the top panel of Figure 2, we show optical–NIR HST images around $z6.1/6.2$ and $z6.3$. From the line peak positions, we identify clear counterparts in the optical–NIR images within a spatial offset of ~$0''1$ for both $z6.1/6.2$ and $z6.3$. Both counterparts have a noticeable dropout feature blueward of ~1 μm, with the one near $z6.1/6.2$ exhibiting a highly elongated shape, aligned with the elongated shape in the 268.684 GHz line. In the highly

elongated object near $z6.1/6.2$, we identify a compact source at the center, whose optical–NIR color is distinct from the other parts of the elongated object, and is indicative of a chance overlapping foreground object. We carefully model and subtract this foreground object (see Appendix C) to study the elongated object near $z6.1/6.2$ in the subsequent analysis. Northeast of $z6.3$, we also identify a nearby compact object. This has a photometric redshift of $0.50^{+0.05}_{-0.32}$ (V. Kokorev et al. 2021, in preparation), and is presumably one of the member galaxies of RXCJ0600-2007 ($z = 0.43$), but does not affect the photometry of $z6.3$.

We conduct optical–NIR photometry and spectral energy distribution (SED) analyses for these counterparts. We also perform aperture photometry, and summarize our results in Table 2. The procedure for aperture photometry is described in detail in Appendix C. With the aperture photometry results, we conduct SED fitting using the EAZY code (Brammer et al. 2008).[33] We fit the photometric flux densities and their uncertainties with linear combinations of templates derived from Brammer et al. (2008), but adopting Flexible Stellar Population Synthesis models as their basis (Conroy et al. 2009; Conroy & Gunn 2010). We adopt the dust attenuation law of Kriek & Conroy (2013) with $\delta = 0$ (i.e., a Calzetti et al. 2000 shape with an additional 2175 Å dust feature).

In Figure 2, we show probability distributions of photometric redshifts for the optical–NIR counterparts of $z6.1/6.2$ and $z6.3$.

---

[33] http://github.com/gbrammer/eazy-py

Table 1
Observed FIR Properties of Bright [C II] Line Emitters Identified in RXCJ0600−2007

Name	z6.1/6.2 (arc)[a]	z6.3	z6.4	z6.5[c]
R.A.	06:00:09.13	06:00:09.55	06:00:08.58	06:00:05.55
Decl.	−20:08:26.49	−20:08:11.26	−20:08:12.54	−20:07:20.86
S/N	9.2	8.0	3.0	⋯
ν_{center} (GHz)	268.682 ± 0.011	268.744 ± 0.016	(268.744)[b]	⋯
FWHM (km s^{-1})	169 ± 22	181 ± 34	(181)[b]	⋯
$z_{[CII]}$	6.0736 ± 0.0003	6.0719 ± 0.0004	(6.0719)[b]	⋯
$S_{[CII]}$ (Jy km s^{-1}0	4.83 ± 0.62	2.75 ± 0.20	0.44 ± 0.20	–
$L_{[CII]}$ ($\times 10^9 L_{\odot}$)	4.5 ± 0.40	2.3 ± 0.21	0.42 ± 0.19	⋯
$f_{1.2mm}$ (mJy)	0.35 ± 0.08	0.20 ± 0.08	<0.16	⋯
[C II] major-axis ($''$)	4.24 ± 0.82	1.17 ± 0.29	⋯[b]	⋯
[C II] minor-axis ($''$)	0.63 ± 0.51	0.88 ± 0.43	⋯[b]	⋯
[C II] position angle ($°$)	71 ± 5	8 ± 430	⋯[b]	⋯

Notes. S/N: Signal-to-noise ratio at the peak pixel in the natural-weighted map, after velocity integration. The velocity integration range is denoted by the yellow shaded region in the right panel of Figure 1. ν_{center} **& FWHM**: [C II] line peak frequency and full-width-at-half-maximum estimated from a single Gaussian fit. $z_{[CII]}$: Redshift of the [C II] line emission estimated from the frequency peak. $S_{[CII]}$ & $L_{[CII]}$: The velocity-integrated [C II] line intensity and the line luminosity with optimized apertures. Here we adopt a velocity integration range of 1.5 × FWHM. $f_{1.2mm}$: Peak 1.2 mm continuum flux density in a uv-tapered ($2''0 \times 2''0$) map. We provide a 2σ upper limit for z6.4. [C II] major-/minor-axis & position angle: De-convolved spatial size (in FWHM) and position angle of the [C II] line in the velocity-integrated map measured with IMFIT. For z6.1/6.2, we use a uv-tapered ($1''0 \times 1''0$) map to obtain the global scale property.
[a] This source is also referred to as RXCJ0060-arc in Laporte et al. (2021).
[b] We do not perform any profile fitting to the spectrum and the 2D spatial map of z6.4, due to its faintness. We adopt the FWHM and the peak frequency associated with z6.3 to calculate the velocity-integrated intensity of the line.
[c] z6.5 falls outside of the ALCS area coverage.

We find that z6.1/6.2 and z6.3 each have peak probabilities close to $z = 6.0$, in excellent agreement with the bright-line detection at ∼268.7 GHz if the [C II] 158 μm line is at $z = 6.07$. In this case, observed line luminosities, L_{line} (i.e., without the correction of the lensing magnification), are estimated to be $4.5 \pm 0.4 \times 10^9 L_{\odot}$ and $2.3 \pm 0.2 \times 10^9 L_{\odot}$ for z6.1/6.2 and z6.3, respectively. With a standard modified blackbody at $z = 6$, with a peak dust temperature $T_d = 38$ K (e.g., Faisst et al. 2020), and a dust emissivity index $\beta_d = 1.8$ (e.g., Chapin et al. 2009; Planck Collaboration et al. 2011), we also obtain observed values for rest-frame FIR luminosities, L_{FIR}, of $5.8 \pm 1.3 \times 10^{11} L_{\odot}$ and $3.3 \pm 1.3 \times 10^{11} L_{\odot}$, and subsequently obtsin line to rest-frame FIR luminosity ratios of 7.8×10^{-3} and 6.8×10^{-3} for z6.1/6.2 and z6.3, respectively. These ratios are consistent with the typical range of the [C II] line $L_{[CII]}$ and L_{FIR} ratios ($L_{[CII]}/L_{FIR}$) among local galaxies (e.g., Brauher et al. 2008; Díaz-Santos et al. 2013), which also supports the hypothesis of the bright lines at ∼268.7 GHz being the [C II] line. Based on the source redshift at $z = 6.07$, we also confirm that star formation rate (SFR) estimates are consistent, between the SED fitting with the dust-attenuation correction and the summation of the rest-frame UV (L_{UV})and L_{FIR}, following the work of Bell et al. (2005), and scaled to the Chabrier IMF:

$$\text{SFR } [M_{\odot} \text{ yr}^{-1}] = 1.09 \times 10^{-10}(L_{FIR} + 2.2L_{UV}). \qquad (1)$$

Although the z6.3 solution shows a small non-zero probability of being at $z \sim 1$, we also identify a 3.6 μm excess feature in both z6.1/6.2 and z6.3 which is often observed in $z \sim 6$ galaxies, due to the contamination of the strong [O III] λ5007 and Hβ lines (e.g., Roberts-Borsani et al. 2016; Harikane et al. 2018). Therefore, the high-z solution at $z \sim 6$ is likely to be favored. Other possibilities for the bright line, along with the high-z solution, might be CO(16-15) at $z = 5.85$, and CO(17-16) at $z = 6.28$. However, recent ALMA studies derive constraints on ratios of $L_{CO(16-15)}/L_{FIR}$ and $L_{CO(17-16)}/L_{FIR} \lesssim 3 \times 10^{-4}$ among luminous quasars at similar redshifts (Carniani et al. 2019). This indicates that L_{line}/L_{FIR} of

z6.1/6.2 and z6.3 are nearly 1.5 dex higher than the typical range, which argues strongly against the possibility of CO(16-15) and CO(17-16) lines. We thus conclude that z6.1/6.2 and z6.3 are [C II] line emitters at $z = 6.07$. Note that we confirm that the [C II] line solution is further supported by the lens models, intrinsic physical properties (see Sections 3.4 and 3.5), and follow-up Gemini/GMOS spectroscopy (Laporte et al. 2021).

Based on the redshift of $z = 6.07$, we also examine the Lyα line in the MUSE data cube around z6.1/6.2 and z6.3. We do not identify any Lyα features around either z6.1/6.2 or z6.3. With the rest-frame UV luminosity, this provides 3σ upper limits for the Lyα equivalent width (EW$_{Ly\alpha}$) at 4.4 Å and 3.7 Å for z6.1/6.2 and z6.3, respectively. Given the dust continuum detection and the redshift, the absence of the bright Lyα line would be ascribed to dust and/or neutral hydrogen in interstellar and intergalactic media. This emphasizes the importance of the ALMA blind line search, which facilitates studies of galaxies irrespective of their Lyα line properties, in particular in the epoch of reionization.

3.3. Mass Model

To study the intrinsic physical properties of the [C II] line emitters z6.1/6.2 and z6.3, we construct several mass models for the galaxy cluster RXCJ0600-2007 ($z = 0.430$) using independent algorithms, including GLAFIC (Oguri 2010), LENSTOOL (Jullo et al. 2007), and Light-Traces-Mass (LTM; Zitrin et al. 2015). Multiple images are selected based on the morphology and colors of galaxies in the HST images captured using RELICS, and guided by y mass models. These models also exploit the MUSE spectroscopic redshift catalog (see Section 2.2) for redshift information relating to some multiple image systems, as well as secure identifications of cluster member galaxies. These models adopt nearly identical sets of multiple image systems to construct their mass models, and provide almost consistent predictions for multiple image
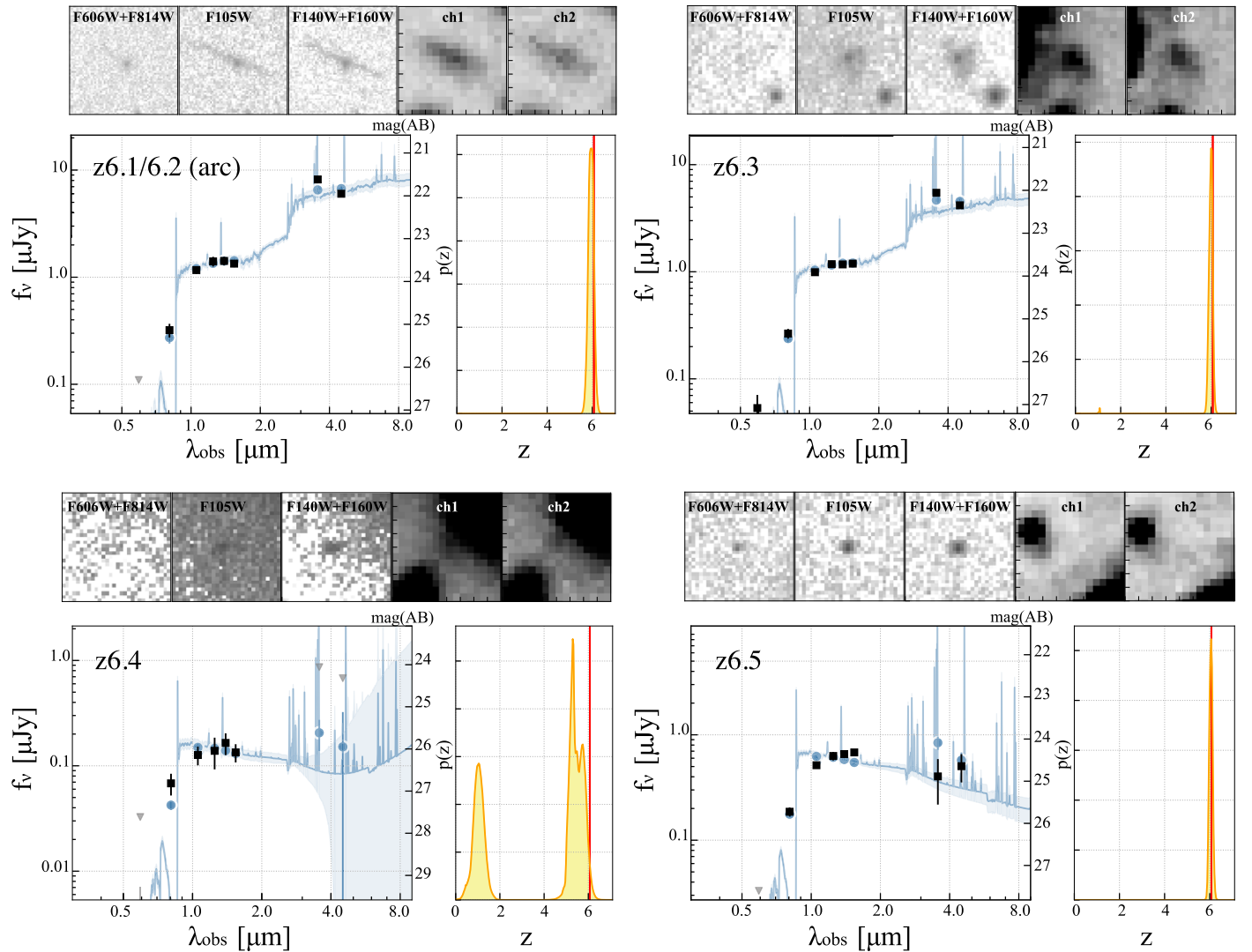
Figure 2. Observed optical–NIR properties of $z6.1/6.2$, $z6.3$, $z6.4$, and $z6.5$, consistently predicted as multiple images of a background LBG at $z \sim 6$ from different mass models (except for $z6.5$, whose identification as a multiple image is tentative). Top: cutouts of the HST ($3'' \times 3''$, except for $z6.1/6.2$ with $6'' \times 6''$) and Spitzer ($8'' \times 8''$) images. Some of the HST images are integrated. The filter name is presented at the top. Bottom: HST and Spitzer photometry (black square) and the best-fit templates, where gray triangles indicate the upper limits. The sum of individual EAZY templates is shown in the light blue curve. The yellow shaded region is the probability distribution of the photometric redshift $p(z)$ from the SED fit. The red line indicates the spectroscopic redshift from the [C II] lines at ~ 268.7 GHz. A 3.6 μm excess feature in $z6.1/6.2$ and $z6.3$ is explained by the contamination of the strong [O III]$\lambda 5007$ and Hβ lines often observed in $z \sim 6$ galaxies (e.g., Roberts-Borsani et al. 2016; Harikane et al. 2018).

positions and magnification factors. A brief summary of these mass models is also presented in Laporte et al. (2021), while full details will be given in a separate paper (in preparation). In this paper, we adopt the mass model of GLAFIC as a fiducial model for our analyses; its construction is described below, although we also use results of LENSTOOL and LTM models to evaluate uncertainties in magnification factors.

We construct a mass model using GLAFIC, in the same manner as Kawamata et al. (2016). Our mass model consists of cluster-scale halos and cluster member galaxies. We place the cluster-scale halos at the positions of the three brightest cluster member galaxies in the core of the cluster. The position of one of the three cluster-scale halos is treated as a free parameter, whereas those of the other two cluster-scale halos are fixed to the galaxy positions. The cluster-scale halos are modeled via an elliptical Navarro–Frenk–White (NFW; e.g., Navarro et al. 1997) profile. The cluster member galaxies are selected using photometric redshifts of galaxies measured from HST images

(Coe et al. 2019) together with galaxy colors. The position and shapes of the member galaxies are fixed to those derived from the HST image, and treat their velocity dispersions and truncation radii using a pseudo-Jaffe ellipsoid as model parameters, assuming a scaling relation (see Kawamata et al. 2016, for more details). In order to achieve a good fit, a member galaxy located at (R.A., decl.) = (06:00:10.664, −20:06:50.65) that produces multiple images is treated as a separate component, again assuming a pseudo-Jaffe ellipsoid. An external shear term, which provides a modest improvement in the mass modeling result, is also included in the mass modeling of this cluster. Having included the multiple images presented in Section 3.4, confirmed with help of our preliminary mass models, we have the positions of 26 multiple images for eight sets of multiple image systems (five multiple image sets with spectroscopic redshifts) that we then adopt as constraints. We optimize the parameters of the mass model based on a standard χ^2 minimization, and determine the best-fit

Table 2
Observed HST and IRAC Photometry of the Multiple Images of RXCJ0600-z6

ID	F606W (μJy)	F814W (μJy)	F105W (μJy)	F125W (μJy)	F140W (μJy)	F160W (μJy)	3.6μm (μJy)	4.5 μm (μJy)
z6.1/6.2 (arc)	<0.07	0.32 ± 0.04	1.17 ± 0.07	1.41 ± 0.13	1.42 ± 0.11	1.34 ± 0.07	8.18 ± 0.42	6.02 ± 0.34
z6.3	0.05 ± 0.02	0.27 ± 0.02	0.99 ± 0.03	1.18 ± 0.06	1.17 ± 0.05	1.19 ± 0.03	5.46 ± 0.20	4.17 ± 0.17
z6.4	<0.02	0.07 ± 0.02	0.13 ± 0.03	0.14 ± 0.05	0.17 ± 0.04	0.13 ± 0.03	<0.59	<0.46[a]
z6.5	<0.02	0.19 ± 0.02	0.51 ± 0.03	0.63 ± 0.05	0.66 ± 0.04	0.68 ± 0.03	0.40 ± 0.18	0.50 ± 0.15

Note. The photometry is performed with separate strategies for four lensed images to account for the crowded cluster field and varying degrees of extended source morphology (see Appendix C). For nondetection, we list the upper limit at the 2σ level.

[a] We obtain 0.34 ± 0.23 μJy which we replace the 2σ upper limit.

mass model, assuming a positional error of $0''6$ for each multiple image to account for perturbations by substructures in the cluster that are not included in our mass model, and estimate the statistical error using the Markov chain Monte Carlo method. Our best fitting model has $\chi^2 = 20.0$ for 17 degrees of freedom. Interested readers are referred to Kawamata et al. (2016) for more specific mass modeling procedures using GLAFIC.

Note that we do not include the foreground object overlapping $z6.1/6.2$ in our mass models, owing to the absence of its spectroscopic redshift. We will discuss the potential contribution of the foreground object to the morphology and magnification factor of $z6.1/6.2$ in Section 4.1.

3.4. Multiple Images

From all of our mass models, we consistently obtain the following two predictions: (i) $z6.1/6.2$ consists of a pair of multiple images of a galaxy at $z \sim 6$ behind RXCJ0600-2007, and (ii) $z6.1/6.2$ and $z6.3$ are also multiple images of the galaxy. The prediction of (ii) is consistent with the [C II] morphology with two close peaks. In fact, we confirm in Appendix D that [C II] line spectra produced at these two peaks show line profiles consistent with each other. In addition, almost the same optical–NIR SED shapes between $z6.1/6.2$ and $z6.3$ in Figure 2 support the prediction of (ii). Although we identify the slight velocity shift between $z6.1/6.2$ and $z6.3$ by $69 \pm 22 \, \mathrm{km \, s^{-1}}$ (see Section 3.1), the offset is much smaller than the typical FWHM range of the [C II] line among $z \sim 4$–6 galaxies evaluated in the ALPINE survey (~ 120–$380 \, \mathrm{km \, s^{-1}}$; Béthermin et al. 2020), suggesting that the slight velocity shift is explained by the differential magnification at different regions of the galaxy. We thus interpret $z6.1/6.2$ and $z6.3$ as multiple images of the [C II] line emission at $z = 6.07$ from a Lyman-break galaxy (LBG) behind RXCJ0600-2007. Hereafter we refer to the background LBG as RXCJ0600-z6.

Subsequently, the different models also predict two additional multiple images of RXCJ0600-z6, the positions of which we present in Figure 1, where we identify corresponding optical–NIR objects. We refer to these potential multiple images as $z6.4$ and $z6.5$. Note that different mass models predict a consistent position for $z6.4$, while predicting different positions for $z6.5$, with a scatter in a $\sim 12''$ scale. In this paper, we focus an optical–NIR object as $z6.5$, as predicted by one of our mass models, but this should be regarded as tentative, as we will discuss below.

To investigate whether the multi-wavelength properties of these potential multiple images are similar to $z6.1/6.2$ and $z6.3$, we conduct aperture photometry for $z6.4$ and $z6.5$ in the optical–NIR bands. The detailed procedure for aperture
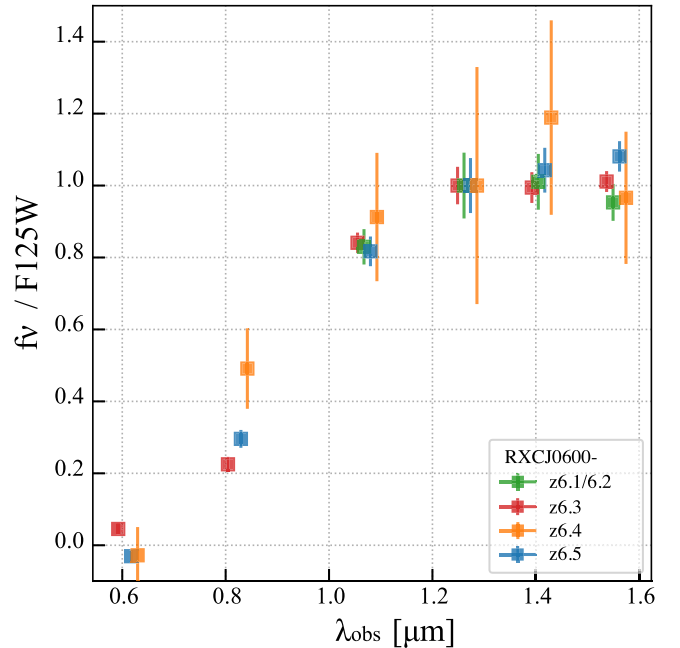

Figure 3. Observed SEDs of the multiple images of RXCJ0600-z6 in the HST bands, normalized by the F125W band. The green, red, brown, and blue squares represent $z6.1/6.2$, $z6.3$, $z6.4$, and $z6.5$, respectively.

photometry is again described in Appendix C. In Table 2 and Figure 3, we summarize the photometry results and the optical–NIR colors normalized by the photometry at the F125W band, respectively. We find that $z6.4$ and $z6.5$ have similar optical–NIR SEDs with $z6.1/6.2$, $z6.3$ within the errors, consistent with our mass model predictions as multiple images at $z \sim 6$. We further perform the optical–NIR SED fitting to $z6.4$ and $z6.5$ in the same manner as $z6.1/6.2$ and $z6.3$. In Figure 2, we also show the optical–NIR SED fitting results of $z6.4$ and $z6.5$. While the $z6.4$ photometry also allows for a $z \sim 6$ solution, the possibility of much lower redshifts cannot be excluded, given the large uncertainties due to its faint characteristics, as well as potential contamination from the nearby BCG (see Appendix C.3). $z6.5$ has a well-localized peak probability at $z \sim 6$, although the HST–Spitzer color of $z6.5$ is much bluer than that seen for the bright images $z6.1/6.2$ and $z6.3$. In fact, an IRAC source at the location of $z6.5$ should be easily detected if it has the same color as those of the other images.

Given that $z6.4$ falls in the ALCS area coverage, we also examine whether the [C II] line emission is detected from $z6.4$ at a frequency consistent with $z6.1/6.2$ and $z6.3$. In Figure 1, we also show the ALMA Band 6 spectrum of $z6.4$, based on an optimized aperture with a radius of $1''5$. We find that $z6.4$ has a

Table 3
Observed Physical Properties of the Multiple Images of RXCJ0600-z6

ID	$z_{\rm phot}$	$z_{\rm spec}$	$M_{\rm UV}$ (mag)	SFR ($M_\odot$ yr^{-1})	$M_{\rm star}$ ($\times 10^9 \, M_\odot$)	A_v (mag)	$\mu_{\rm whole}$[a]	$\mu_{\rm local}$[a]
z6.1/6.2 (arc)	$5.95^{+0.11}_{-0.13}$	6.0734 ± 0.0003	-23.23 ± 0.07	135^{+45}_{-23}	$41.9^{+0.4}_{-10.1}$	$0.07^{+0.11}_{-0.05}$	29^{+4}_{-7}	163^{+27}_{-13}
z6.3	$5.99^{+0.07}_{-0.09}$	6.0719 ± 0.0004	-23.06 ± 0.06	114^{+11}_{-26}	$20.1^{+1.8}_{-2.7}$	$0.18^{+0.09}_{-0.11}$	21^{+14}_{-7}	...
z6.4	$5.25^{+0.48}_{-4.24}$	(6.0719)	-21.02 ± 0.11	$2.6^{+1.2}_{-0.1}$	$0.23^{+0.12}_{-0.01}$	$1.80^{+2.25}_{-1.78}$	$3.3^{+2.4}_{-1.2}$	...
z6.5	$6.05^{+0.07}_{-0.07}$	...	-22.48 ± 0.05	$8.7^{+0.7}_{-0.1}$	$0.77^{+0.05}_{-0.01}$	$0.03^{+0.12}_{-0.01}$	$4.2^{+1.8}_{-1.3}$	...

Note. Physical properties obtained from the SED fitting of the observed photometry with EAZY without correcting for the lensing magnification. The intrinsic physical properties after the correction of the lensing magnification are summarized in Table 4. Based on the conversion from the UV and FIR luminosity of Bell et al. (2005), scaled to the Chabrier IMF, we obtain consistent SFR estimates of $188 \pm 15 \, M_\odot$ yr^{-1} and $120 \pm 14 \, M_\odot$ yr^{-1} for z6.1/6.2 and z6.3, respectively. Since UV luminosity dominates in both z6.1/6.2 and z6.3, a ± 10 K difference in the $T_{\rm d}$ assumption for the $L_{\rm FIR}$ calculation (Section 3.2) changes these SFR estimates by ~ 0.1 dex.
[a] We define $\mu_{\rm whole}$ and $\mu_{\rm local}$ as follows: $\mu_{\rm whole}$ = (observed luminosity of the multiple image)/(overall luminosity of the intrinsic galaxy); $\mu_{\rm local}$ = (observed luminosity of the multiple image)/(local luminosity of the strongly lensed, sub region near the caustic line), where the sub region corresponds to the dashed rectangle area in Figure 4. The errors are evaluated on the basis of the minimum to maximum range among our independent mass models.

tentative line detection (3.0σ) at a frequency consistent with z6.1/6.2 and z6.3. Moreover, z6.4 has an asymmetry line profile (the brighter peak at the higher frequency side) which is consistent with the line profile of z6.3. These results strengthen the case that z6.4 is indeed one of the multiple images of the background LBG.

Based on these results, we find that the identification of z6.4 as one of the multiple images is relatively secure in terms of the consistent predictions of the mass models, as well as the line detection at the consistent frequency. On the other hand, based on the different predicted positions among the different mass models, and the disagreements in the HST–Spitzer color with other multiple images, the interpretation of z6.5 being another multiple image is not secure, and should be taken with caution until a spectroscopic redshift is obtained in follow-up observations. We therefore use the positions of z6.1/6.2, z6.3, and z6.4 as constraints in deriving our best-fit mass models. We present the critical curve at $z = 6.07$ from the best-fit mass model of GLAFIC in the left panel of Figure 1. We summarize the [C II] line properties and the SED fitting results for all these multiple images in Tables 1 and 3, respectively.

3.5. Physical Properties of RXCJ0600-z6

The configuration of the multiple images is helpful in obtaining precise information about the source position and its surface brightness profile in the source plane. Here we estimate the intrinsic two-dimensional (2D) surface brightness profile by fitting the HST images, assuming the fiducial mass model. Specifically, we first produce a $1\farcs 7 \times 1\farcs 7$ cutout HST/F160W image of z6.3. With a single Sérsic profile model in the source plane, we then obtain a best-fit effective radius of $r_{\rm e} = 1.2^{+4.1}_{-0.1}$ kpc (major axis), an axis ratio of $0.49^{+0.03}_{-0.02}$, a position angle = $84^{+2}_{-2}°$, a Sérsic index of $n = 2.5^{+1.2}_{-0.1}$, and a central coordinate of (R.A., decl.) = (6:00:08.12, −20:07:39.55), based on standard χ^2 minimization. Since we find a degeneracy between $r_{\rm e}$ and n, we restrict the Sérsic index to the range of $1 < n < 4$ in the fitting in this case. We do not use z6.1/6.2 and z6.4 for the fitting, due to the complicated morphology, and to the contamination of the diffuse emission from the nearby BCG, respectively. We ignore the clumpy structure of z6.3 for the moment, and reserve it for later discussion. We list these best-fit Sérsic profile results in Table 4.

In Figure 4, we show the best-fit 2D Sérsic profile in the source plane, and its multiple images in the image plane. We find that a single Sérsic profile effectively reproduces not only

Table 4
Intrinsic Physical Properties of Strongly Lensed LBG of RXCJ0600-z6

Name	RXCJ0600-z6	
Region	Whole	Sub
Counter image	z6.3	z6.1/6.2
	(1)	(2)
R.A.	06:00:08.11	06:00:08.13
Decl.	−20:07:39.65	−20:07:39.53
$z_{\rm spec}$	6.0719 ± 0.0004	6.0734 ± 0.0003[a]
EW$_{Ly\alpha}^{\rm rest}$ (Å)	< 4.4	< 3.7
$L_{\rm [CII]} (\times 10^8 \, L_\odot)$	$1.1^{+0.7}_{-0.5}$	$0.3^{+0.1}_{-0.1}$
$M_{\rm UV}$ (mag)	$-19.75^{+0.55}_{-0.44}$	$-17.70^{+0.17}_{-0.09}$
SFR ($M_\odot$ yr^{-1})	$5.4^{+4.5}_{-2.9}$	$0.8^{+0.4}_{-0.2}$
$M_{\rm star} (\times 10^8 \, M_\odot)$	$9.6^{+6.0}_{-4.6}$	$2.6^{+0.2}_{-1.0}$
A_v (mag)	$0.18^{+0.09}_{-0.11}$	$0.07^{+0.11}_{-0.05}$
$r_{\rm e}$ (kpc)	$1.2^{+4.1}_{-0.1}$	...
n	$2.5^{+1.2}_{-0.1}$	...
axis ratio	$0.49^{+0.03}_{-0.02}$	...
PA (°)	84^{+2}_{-2}	...
$M_{\rm dyn} (\times 10^9 \, M_\odot)$	3 ± 1	...
$M_{\rm gas} (\times 10^9 \, M_\odot)$	2 ± 1	...
$f_{\rm gas}$ (%)	~ 50–80	...

Note. (1) The physical properties related to the whole region of the galaxy, obtained by applying $\mu_{\rm whole}$ (Table 3) to the observed properties of z6.3. The best-fit Sérsic profile ($r_{\rm e}$, n, and axis ratio) is not estimated by using $\mu_{\rm whole}$, but by optimizing the intrinsic 2D surface brightness profile in the source plane to match the 2D surface brightness profile of z6.3 in the image plane via GLAFIC (see Section 3.5). The circularized effective radius is estimated to be $0.8^{+2.9}_{-0.1}$ kpc, which is consistent to within ~ 1–2σ errors, with an independent 2D surface brightness profile fit on the image plane in Laporte et al. (2021). We calculate $M_{\rm gas}$ by subtracting $M_{\rm star}$ from $M_{\rm dyn}$, which is consistent with another estimate from the empirical calibration with [C II] luminosity (Zanella et al. 2018) of $3 \pm 1 \times 10^9 \, M_\odot$ (see Section 4.2). (2) The physical properties related to the local scale of the galaxy in the sub region near the caustic line, by applying $\mu_{\rm local}$ (Table 3) to the observed properties of z6.1/6.2.
[a] The sub region is redshifted by 69 ± 22 km s^{-1}, which agrees well with the velocity gradient identified in the whole scale of RXCJ0600-z6 (see Section 4.2).

z6.3, but also z6.4 and z6.1/6.2, whose elongated shape is interpreted as a result of the source crossing the caustic line in the source plane and being stretched over $\sim 6''$ scale in the image plane (e.g., Vanzella et al. 2020). This interpretation is consistent with the slight difference in the line peak frequencies and the line profiles between z6.1/6.2 and z6.3 (Section 3.1),
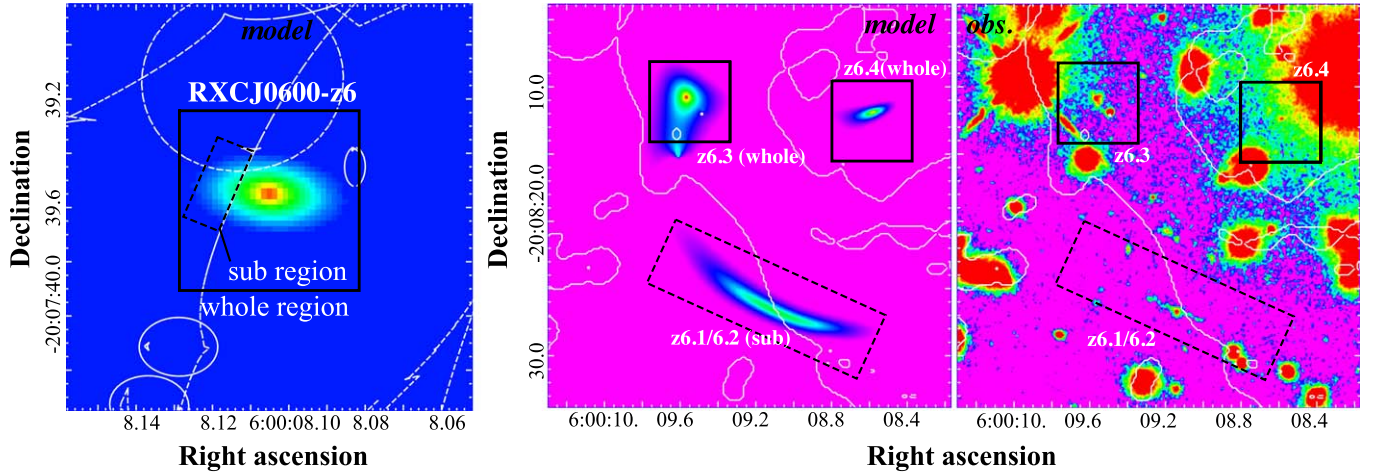
Figure 4. Left: best-fit 2D Sérsic profile (effective radius in major axis = 1.2 kpc, axis ratio = 0.49, Sérsic index n = 2.5) and coordinate (R.A., decl. = 6:00:08.12, −20:07:39.55) of the lensed LBG RXCJ0600-z6 at $z = 6.0719$ in the source plane, based on the fiducial mass model. The fitting is performed based on the standard χ^2 minimization, only with the $1\farcs7 \times 1\farcs7$ HST/F160W cutout of z6.3. The white dashed curves denote the caustic lines at the source redshift. Middle: multiple images of RXCJ0600-z6 in the image plane, z6.1/6.2, z6.3, and z6.4, as predicted by the fiducial mass model with the best-fit 2D Sérsic profile in the left panel. The black boxes show the $6'' \times 6''$ areas around z6.3 and z6.4 at the same positions as the yellow boxes in Figure 1. The dashed black rectangle denotes the $6'' \times 17''$ area around z6.1z6.2, which approximately corresponds to the dashed black rectangle shown in the left panel along the caustic line. The white line indicates the critical curve. Right: HST/F160W image, showing the multiple images of z6.1/6.2, z6.3, and z6.4. The image size is the same as that shown in the middle panel. The color and symbols are assigned in the same manner as the middle panel.

because the sub region of the galaxy can have different kinematic properties, as compared to the whole galaxy. By calculating the ratio of the spatial areas between the source and image planes, the magnification factors for z6.1/6.2 and z6.3 in our fiducial model (average of the three independent models) are estimated to be ∼150 (163) and ∼35 (21), respectively. The observed luminosity of z6.1/6.2 is 33 (29) times brighter than the intrinsic overall luminosity of RXCJ0600-z6, due to the strong gravitational lensing effect near the caustic line. By comparing the physical properties of z6.3 and z6.4 that trace the whole region of the lensed galaxy, we confirm that our independent mass models agree in the ratio of magnification factors between z6.3 and z6.4 in the range of 6.1–6.7, which is consistent with the observed $L_{\rm [CII]}$ ratio of 5.7 ± 2.7 between z6.3 and z6.4. These results validates our best-fit mass models and 2D Sérsic profile in the source plane.

To be conservative, we adopt the average value of the magnification factors, evaluating its uncertainty from the minimum to maximum values among our independent mass models, when we estimate the intrinsic physical properties of RXCJ0600-z6 in this paper. We list the average magnification factor and its uncertainty in Table 3. Applying the average magnification factors to the FIR (Section 3.1) and optical–NIR (Section 3.2) properties, we summarize the intrinsic physical properties in both whole and sub-regions of RXCJ0600-z6 in Table 4. Remarkably, we obtain the intrinsic absolute rest-frame UV magnitude of $M_{\rm UV} = -19.75^{+0.55}_{-0.45}$, which is ∼3 times fainter than the L^* value of the LBG luminosity function at $z = 6$ ($M_{\rm UV} = 20.91^{+0.07}_{-0.06}$; Ono et al. 2018). In Figure 5, we show the SFR and $M_{\rm star}$ relation of RXCJ0600-z6. For comparison, we also present the average relation among the $z \sim 6$ galaxies estimated in Iyer et al. (2018) (gray shaded region). We find that RXCJ0600-z6 falls on the average relation from the sub- to whole regions. We also find that the relation between the [C II] line width and luminosity in RXCJ0600-z6 agrees with the average value among $z \sim 6$ galaxies, as well as the theoretical prediction (see Figure 10 in Kohandel et al. 2019). The circularized effective radius
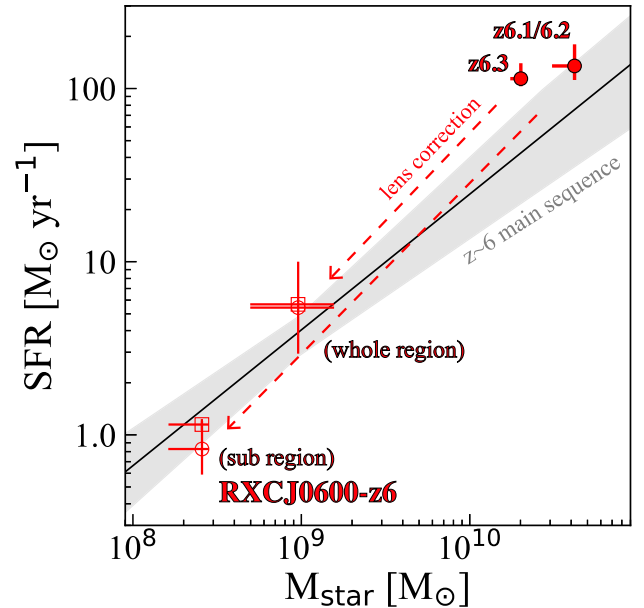

Figure 5. SFR–$M_{\rm star}$ relation. The red filled and open circles indicate the relations before and after applying the correction of the lensing magnification to the SED fitting results, respectively, for z6.1/6.2 and z6.3. The errors include the uncertainty from the mass models (Table 3). The red open squares indicate SFR estimates after lensing magnification correction, based on the conversion from the UV and FIR luminosity of Bell et al. (2005), scaled to the Chabrier IMF. The black line and the gray shaded region denote the best-fit relation for $z \sim 6$ galaxies and its 1σ uncertainty, as evaluated in Iyer et al. (2018).

($r_{\rm e,circ} \equiv r_{\rm e} \times \sqrt{\rm axis\ ratio}$) of 0.84 kpc also falls within a typical range among $z \sim 6$ galaxies with similar UV luminosity (see e.g., Figure 9 of Kawamata et al. 2018). These results indicate that RXCJ0600-z6 is an abundant, representative sub-L^* galaxy at this epoch. We note that these intrinsic physical properties are consistent with independent estimates in Laporte et al. (2021) within the errors, even though the SED fitting strategies are different, due to the respective scope of each paper.

9

4. [C II] Views from ISM to Cosmic Scales

The uniquely and strongly lensed galaxy near the caustic line (Section 3.3) allows us to study ISM properties from internal to whole scales in the host galaxy. For an example of the whole view of the galaxy based on $z6.3$, the spatial resolutions of the HST map of $\sim 0''2$ translate into $0''04$ (corresponding to ~ 250 pc at $z = 6.07$) after the correction of the lensing magnification, providing sub-kpc scale ISM views. At the same time, the blind aspect of the ALCS survey also allows us to statistically evaluate the number density of the [C II] line emitters at $z \sim 6$ in a cosmic scale, based on our successful identification of RXCJ0600-z6. In conjunction with the rest-frame UV and FIR continuum properties, we examine the [C II] line properties from the ISM to cosmic scales, and discuss the existence of common properties or a large diversity between these multiple scales.

4.1. Spatial Distributions of UV, FIR, and [C II] Down to Sub-kpc Scale

Making full use of gravitational lensing, we investigate the spatial distributions of the [C II] line, rest-frame UV, and FIR continuum on the source plane, and compare them. In the context of similar studies so far at $z \sim 2$–4 for bright, dusty, starburst galaxies (e.g., Swinbank et al. 2010, 2015; Dye et al. 2015; Spilker et al. 2016; Rybak et al. 2015; Tamura et al. 2015; Hatsukade et al. 2015; Rybak et al. 2020; Rizzo et al. 2020), and less massive galaxies (e.g., Dessauges-Zavadsky et al. 2017, 2019), this is a first observation to resolve the ISM structure down to the sub-kpc scale for the sub-L^* galaxy in the epoch of reionization.

In the left panel of Figure 6, we present the rest-frame UV continuum maps for $z6.3$ (i.e., whole region) and $z6.1/6.2$ (i.e., sub region) in the HST/F160W band, with the [C II] line (red contour) and the rest-frame FIR continuum (green contour) captured by ALMA. The emission peaks of the [C II] line and rest-frame FIR continuum are marked with red and green squares (triangles) for $z6.3$ ($z6.1/6.2$), and with 1σ error bars,[34] respectively. Here we do not examine the rest-frame FIR continuum peak from $z6.3$, due to its poor significance at the 2.5σ level (see Section 3.1). In $z6.3$, the rest-frame UV continuum shows a clumpy structure, and we duly mark these clumps with black crosses labeled a, b, and c, from brightest to faintest. The rest-frame UV continuum of $z6.3$ also shows an elongated structure toward the north east, which we mark with an additional black cross and label d. In $z6.1/6.2$, possible clumps are more evident in the [C II] line and the rest-frame FIR continuum with the two-peak morphology. If RXCJ0600-z6 consists of a smooth disk, the morphology of $z6.1/6.2$ would be a single smooth arc shape, as shown in the middle panel of Figure 4. Therefore, the two-peak morphology of $z6.1/6.2$ may imply that the ISM of RXCJ0600-z6 near the caustic line has a clumpy structure in the source plane. An alternative possibility is that an intrinsically smooth disk is stretched into the two-peak morphology in the image plane, due to perturbation from the foreground object overlapping $z6.1/6.2$, which is not included in our fiducial mass model. To check

this possibility, we include the foreground object in our mass model, assuming that it is a member galaxy of the cluster (see Appendix C.2), finding that the two-peak structure can indeed be reproduced, if the mass associated with the foreground object is comparable or larger than that expected from the scaling relation of the luminosity and mass for cluster member galaxies constrained in our mass modeling. We conclude that we need more follow-up data, including the spectroscopic redshift of the foreground object, in order to discriminate these two possibilities. We confirm, however, that both magnification factors of μ_{local} and μ_{whole} for $z6.1/6.2$ are affected only by $\sim 1\%$–2%, even if we include the foreground object in the mass model as one of the cluster members or outside of the cluster up to $z \sim 4$. The other foreground object near $z6.3$ is classified as one of the member galaxies of the cluster (Section 3.2), and is predicted to produce the critical curve at the southern east part of $z6.3$ in our mass model (see the middle panel of Figure 4). However, we find that the [C II] morphology at the corresponding area is not disturbed at all, suggesting that its lensing effect is negligible for $z6.3$. We therefore remove this foreground object from the mass model and the HST map with GALFIT in the source plane reconstruction of $z6.3$.

In the right panel of Figure 6, we present the source plane reconstruction of $z6.3$ (whole region), where the inset panel displays the source plane reconstruction of $z6.1/6.2$ (sub-region). To match the spatial resolution between HST and ALMA, we create a [C II] map from the de-convolved [C II] spatial distribution (Section 3.1), smooth it with the point-spread function (PSF) of the HST F160W band, and use this PSF-matched map for the source plane reconstruction of the [C II] line. In the right panel, the white ellipses indicate the source plane reconstruction of the HST PSF, whose FWHM is decreased down to $\sim 200 \times 100$ pc and $\sim 300 \times 60$ pc around $z6.3$ and $z6.1/6.2$, respectively. The other colors and symbols follow the same assignment as the left panel, where we also apply the lens correction to the error bars. The error bar of the [C II] line peak position in $z6.3$ (red square) decreases to ~ 300 pc. These results indicate that we are able to map the ISM view down to the scale of a few hundred parsecs. Note that our independent mass models consistently suggest that the two-peak morphology of $z6.1/6.2$ in the image plane are a pair of multiple images (Section 3.3), regardless of the presence or absence of a foreground object, and thereby correspond to one peak in the source plane. We confirm that the entire morphology in both whole and sub-regions of the galaxy, as well as the emission peak positions, do not change beyond the errors in the source plane whether or not we include the foreground galaxy overlapping $z6.1/6.2$ in the mass model as one of the member galaxies of RXCJ0600-2007.

Firstly, from the reconstruction of $z6.3$, we find that, on the galxy scale, the [C II] line peak shows an offset of $\simeq 300$ pc from the brightest rest-frame UV clump of a, but is consistent at the 1σ error level. With an axis ratio of 0.49 (see Table 4), nonparametric measurements directly on the surface brightness distributions in the source plane provide $r_e = 1.1$ kpc and 2.6 kpc for the rest-frame UV continuum and the [C II] line emission, respectively, indicating a [C II] gas structure spatially extended by a factor of ~ 2.4. These results are consistent with the recent ALMA results of Fujimoto et al. (2020b) for 23 individual normal star-forming galaxies at $z \sim 4$–6, whereby generally the [C II] line is spatially more extended than the rest-frame UV continuum by a factor of ~ 2–3 without a spatial

---

[34] The error is estimated by the approximate positional accuracy of the ALMA map, Δp, in milliarcsec, given by $\Delta p = 70,000/(\nu^* B^* \sigma)$, where σ is the peak SNR in the map, ν is the observing frequency in GHz, and B is the maximum baseline length in kilometers (see Section 10.5.2 in cycle 7 ALMA technical handbook)
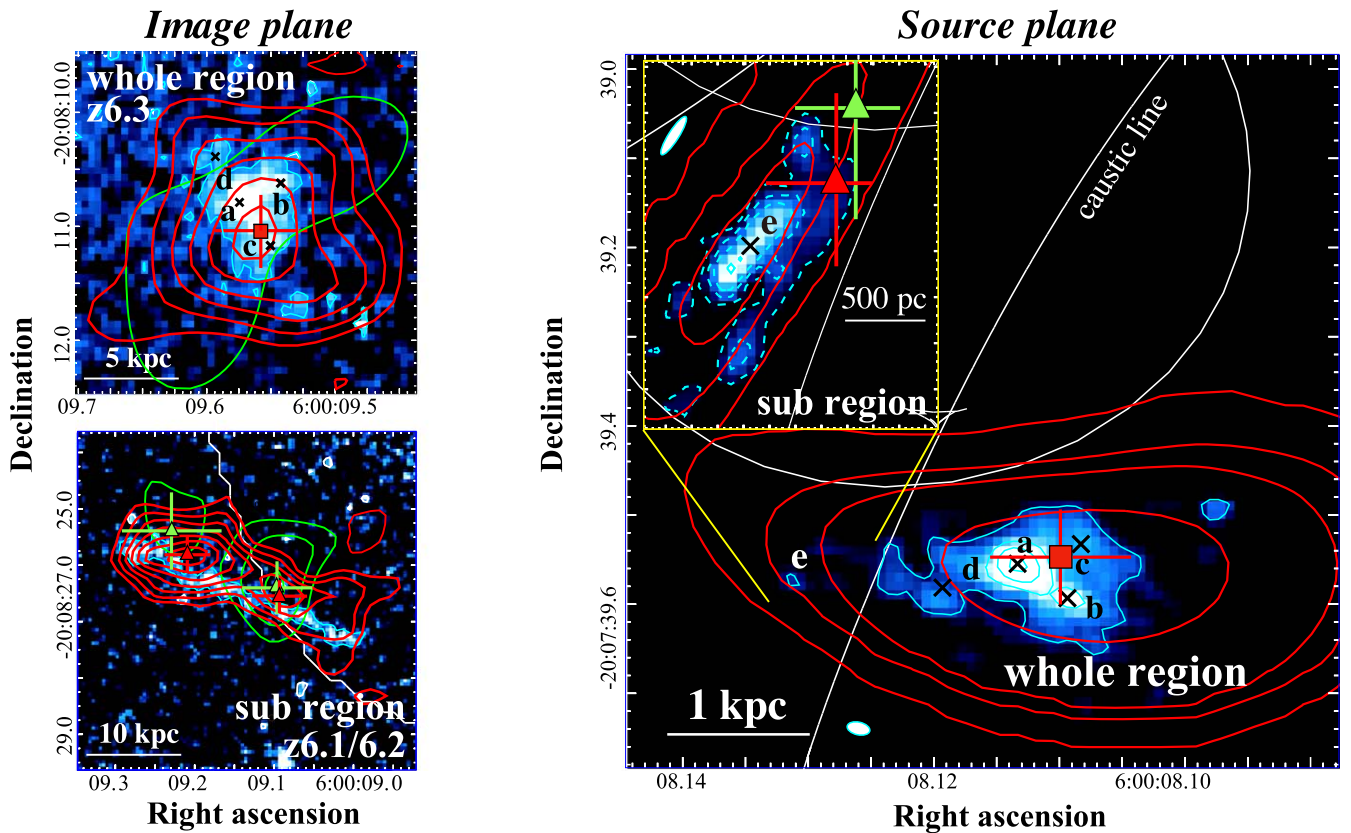
Figure 6. Left: $3'' \times 3''$ and $6'' \times 6''$ HST/F160W cutouts of $z6.3$ (top) and $z6.1/6.2$ (bottom) in the image plane. The small black crosses denote bright clumps (marked a, b, and c) and an elongated structure toward north east (d) in the rest-frame UV continuum. The dashed black cross indicates the peak position of the rest-frame UV continuum after smoothing the HST map to match the resolution with ALMA. The red and green contours represent the [C II] line and the rest-frame FIR continuum from ALMA, drawn at 1σ intervals from 2σ to 8σ. The red and green squares (triangles) in $z6.3$ ($z6.1/6.2$) show the emission peak pixel positions of the [C II] line and rest-frame FIR continuum with 1σ error bars, respectively. The cyan contours are drawn at 2σ for the rest-frame UV continuum. The foreground galaxies are removed with GALFIT for the purpose of source plane reconstruction. Here we use the natural-weighted map for the [C II] line, and the uv-tapered maps with $2''0 \times 2''0$ and $0''8 \times 0''8$ for the rest-frame FIR continuum of $z6.3$ and $z6.1/6.2$, respectively. Right: source plane reconstruction of the [C II] line and rest-frame UV and FIR continuum of $z6.3$. The color and symbols follow the same assignment as the left panel, where the cyan and red contours show 10%, 30%, 50%, and 80% of the peak. To match the spatial resolutions of ALMA and HST, the red contours are drawn from the source plane reconstruction of the de-convolved [C II] spatial distribution obtained with IMFIT (Section 3.1), and smoothed using the HST PSF. The inset panel displays the source plane reconstruction of $z6.1/6.2$. The cyan (red) contours show 1%, 3%, 5%, and 10% (10%, 30%, and 50%) of the peak of the whole galaxy, respectively. The luminosity-weighted center is marked with the label e, corresponding to the faint rest-frame UV clump at the western part of the whole galaxy. The white ellipses show the typical shape of the HST PSF reconstructed in the source plane. The error bars of the red square, triangle, and green triangle incorporate the average lensing magnification corrections and their uncertainties. Note that the two peaks (= triangles) in $z6.1/6.2$ in the image plane constitute a multiple pair (Section 3.3), which thereby correspond to one peak (= triangle) in the source plane.

offset beyond $\simeq$ a 1 kpc scale. The r_e value for the rest-frame UV continuum is also consistent with the Sérsic profile fitting results of 1.2 kpc in the source plane presented in Section 3.5.

Secondly, from the reconstruction of $z6.1/6.2$, we find in the sub-region of the galaxy that the [C II] line is again co-spatial with the rest-frame UV continuum, which is separated by $\sim$1.6 kpc from the peak of the [C II] line and rest-frame UV continuum from the whole region of the galaxy. We mark the luminosity-weighted center of the sub-region with a black cross labeled e. Remarkably, we find, in the independent rest-frame UV continuum map reconstructed from $z6.3$, that the faint clump exists at exactly the position of e, whose peak flux density is also consistent. These agreements in the properties of clump e also support the robustness of our best-fit mass models. We also find that the [C II] and rest-frame FIR peaks observed in the image plane are reconstructed in the source plane with a $\simeq$1 kpc offset from the luminosity-weighted center of e. This indicates that the faint diffuse emission or further faint clump near the caustic line is strongly lensed and more prominently visible in the image plane than clump e. Given that RXCJ0600-

$z6$ is quantified by $r_e = 1.2$ kpc in the rest-frame UV continuum (Section 3.5), these results indicate that we are witnessing very faint [C II] and rest-frame FIR-emitting region(s) near the caustic line beyond the effective radius of the galaxy which is almost invisible in other multiple images. Because of the poor significance level of the rest-frame FIR continuum in $z6.3$, we cannot conclude whether the rest-frame FIR continuum detected in $z6.1/6.2$ corresponds to the outskirt emission of the whole galaxy or the localized emission at the sub region of the galaxy.

Interestingly, the brightest peaks of the [C II] line and the rest-frame FIR continuum in $z6.1/6.2$ appear on opposite sides in the image plane (Left bottom panel of Figure 6). In $z6.1/6.2$, the magnification factor is generally the same on either side. The clear difference identified in the [C II] line strength at high significance levels (8.2σ and 5.4σ) suggests the existence of a substructure of the mass distribution along the line-of-sight of $z6.1/6.2$, i.e., the so-called *flux-ratio anomaly* (e.g., Mao & Schneider 1998). This is consistent with our interpretation that the central compact object in the optical–NIR bands in $z6.1/6.2$
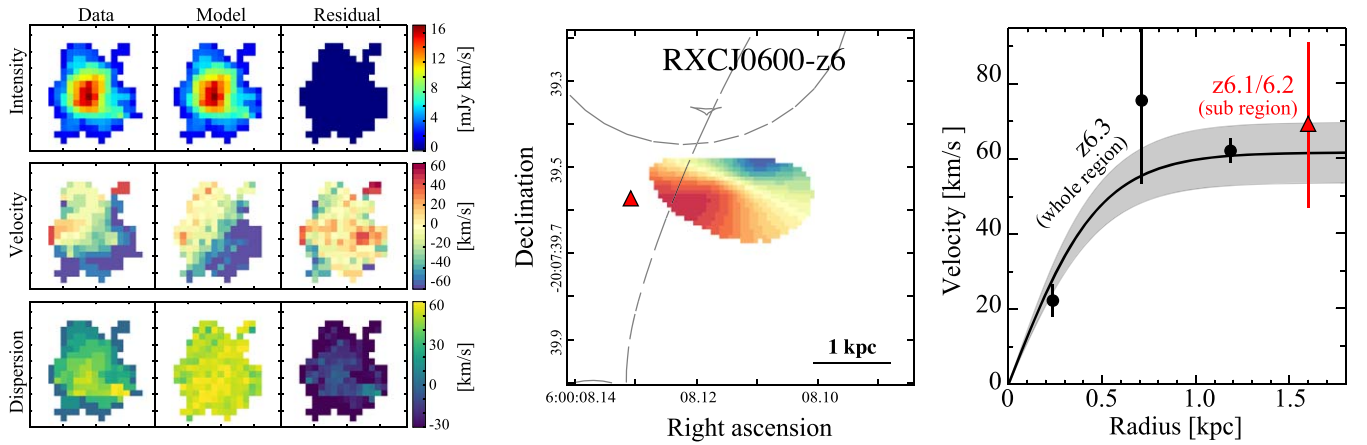
Figure 7. Kinematic properties of RXCJ0600-z6. Left: velocity-integrated (i.e., intensity; top), velocity-weighted (middle), and velocity-dispersion (bottom) maps of z6.3 are shown in the left column. The best-fit 3D model with ^{3D}BAROLO, together with the residual maps, are presented in the middle and right columns, respectively. The image size is $3'' \times 3''$. Middle: source plane reconstruction of the intrinsic velocity-weighted map of z6.3, obtained using GALPAK3D. We limit the reconstruction up to the radius of $1''4$ from the [C II] intensity peak in the image plane. The gray dashed line is the caustic line. The red triangle shows the luminosity-weighted center of the sub region of the galaxy. Right: observed radial velocity profile of z6.3, extracted from the three annuli defined for the ^{3D}BAROLO analysis (black circles), with the spatial and velocity offsets of the sub region of the galaxy observed in z6.1/6.2 (red triangle). The black line shows the best-fit, together with the associate 1σ error (gray shade), of the radial velocity profile of z6.3 obtained from GALPAK3D.

is the foreground object responsible for this *flux-ratio anomaly*. However, if the [C II] and rest-frame FIR-emitting regions are identical in the source plane, the flux ratio should be the same between the [C II] and rest-frame FIR emission in the image plane. Although the current error bars of the spatial positions are large, this independent observable of the flux ratio suggests that the faint [C II] and rest-frame FIR-emitting regions are physically offset in the sub-region of RXCJ0600-z6. This potential separation, and the detailed ISM structure in RXCJ0600-z6 must be addressed in future deeper and higher-resolution observations.

4.2. Kinematics via [C II]

We also examine the kinematics of RXCJ0600-z6 via the bright [C II] line emission. Here we focus on the [C II] kinematics of z6.3 to characterize the gas kinematics of the whole galaxy. In the left panel of Figure 7, we present velocity-integrated (top), velocity-weighted (middle), and velocity-dispersion (bottom) maps of z6.3 in the image plane. We evaluate the root-mean-square noise level from the data cube and create these maps with a three-dimensional (3D) mask of all signals above the the 2σ level. We find that the [C II] line has a velocity gradient from -100 to $+45$ km s^{-1} in east south to west north, with its intensity extended up to a radius of $\sim 1''4$. Assuming the line width estimate of z6.3 (Table 1), and a potential error of ~ 30 km s^{-1} for the velocity gradient due to the spectral resolution of our ALMA data cube (Section 2.1), we obtain $\Delta v_{obs}/2\sigma_{tot} = 0.94 \pm 0.26$, where Δv_{obs} and σ_{tot} are the full observed velocity gradient (uncorrected for inclination) and the spatially-integrated velocity dispersion, respectively. With an approximate diagnostic for the classification of rotation-dominated and dispersion-dominated systems, whereby $\Delta v_{obs}/2\sigma_{tot} = 0.4$ (Förster Schreiber et al. 2009), we find that z6.3 is classified as a rotation-dominated system. Note that the beam smearing effect generally causes the velocity gradient [dispersion] to be underestimated [overestimated] in spatially low-resolution maps (see e.g., Figure 7 of Di Teodoro & Fraternali 2015). This strengthens the argument that z6.3 is a rotation-dominated

system, on the basis of the increased $\Delta v_{obs}/2\sigma_{tot}$ value without the beam smearing effect.

To study the rotation kinematics, we analyze our data in the image plane using the ^{3D}BAROLO (Di Teodoro & Fraternali 2015) and GALPAK3D (Bouché et al. 2015) software packages; these are tools for fitting 3D models to emission-line data cubes. In the left panel of Figure 7, we also show the best-fit 3D model and residual maps using ^{3D}BAROLO, assuming three annuli for its tilted ring fitting algorithm. We find an excellent agreement on the intensity map, and that the residual velocities in velocity-weighted and velocity-dispersion maps are generally below the spectral resolution of our ALMA data cube (~ 28 km s^{-1}; Section 2.1). Although the residual in the velocity dispersion is relatively large near the edge of the mask, this is likely to be because the faint outskirt emission near the edge is masked in some velocity channels, and the observed velocity dispersion is underestimated. These results suggest that the [C II] kinematics of z6.3 are well reproduced by the best-fit 3D model. We confirm that an independent 3D modeling of a single exponential disk with GALPAK3D also provides the best-fit values of the rotation velocity, the velocity dispersion, and the inclination, fully consistent within errors with the ^{3D}BAROLO results. We summarize the details of the 3D modeling and the results in Appendix E.

In the middle panel, we present the velocity-weighted map of z6.3 in the source plane via a reconstruction performed in the same manner as in Section 4.1. To understand the intrinsic picture without the beam smearing effect, here we use the best-fit intrinsic (i.e., resolution free) map obtained from GALPAK3D for the reconstruction. In the right panel, we also show the [C II] radial velocity extracted from the three annuli with ^{3D}BAROLO (black circle), as well as the best-fit (black line) and the 1σ error (gray shade) of the rotation curve in the tanh formalization obtained from GALPAK3D. The correction of the lensing magnification is applied to the radius scale. For comparison, the spatial and velocity offsets of z6.1/6.2 are denoted by a red triangle in both middle and right panels. We find that z6.1/6.2 agrees with the velocity gradient of z6.3 within the errors, which is consistent with our interpretation that z6.1/6.2 is a sub region of RXCJ0600-z6. This suggests

that clump e in the sub region of the galaxy (Section 4.1) is likely to be a small star-forming region within the rotation disk of the host galaxy.

For the rotation-dominated system, we obtain a dynamical mass, M_{dyn}, of $(3 \pm 1) \times 10^9 \, M_\odot$ based on an assumption of disk-like gas potential distribution, following Equation (4) in Dessauges-Zavadsky et al. (2020):

$$\left(\frac{M_{dyn}}{M_\odot}\right) = 1.16 \times 10^5 \left(\frac{v_{rot}}{km \, s^{-1}}\right)^2 \left(\frac{r_e}{kpc}\right), \qquad (2)$$

where v_{rot} is the rotation velocity of the gaseous disk after inclination correction. We calculate the inclination from the axis ratio of the best-fit surface brightness profile results for the rest-frame UV continuum (Section 3.5), assuming that the higher-resolution map provides a better constraint for the inclination. We adopt r_e and v_{rot} from the source plane reconstruction of the [C II] line (Section 4.1) and the GALPAK3D results, respectively. We caution that the uncertainty of the inclination could remain at $\sim$30% even in the spatially resolved analysis (e.g., Rizzo et al. 2020), and thus the uncertainty in the above M_{dyn} estimate could be even larger.

Given the negligible contribution of the dark matter halo in the galactic scale, we estimate the molecular gas mass, M_{gas}, to be $\sim$1–2 $\times 10^9 \, M_\odot$ by subtracting M_{star} (Section 3.5) from M_{dyn}. It is worth noting that this M_{gas} range agrees with another estimate, based on an empirically calibrated method, in Zanella et al. (2018), given by

$$\left(\frac{L_{[CII]}}{L_\odot}\right) = 10^{-1.28 \, (\pm 0.21)} \times \left(\frac{M_{gas}}{M_\odot}\right)^{0.98 \, (\pm 0.02)}, \qquad (3)$$

which suggests that $M_{gas} = 3^{+2}_{-1} \times 10^9 \, M_\odot$, despite the potentially large uncertainty of the inclination. These results indicate that RXCJ0600-z6 is a gas-rich galaxy with a high gas fraction of f_{gas} ($\equiv M_{gas}/(M_{star} + M_{gas})) \sim$ 50%–80%. This is consistent with recent ALPINE results, where [C II]-detected ALPINE galaxies with $M_{star} \sim 1 \times 10^9 \, M_\odot$ have $f_{gas} \sim$ 60%–90% (see Figure 8 in Dessauges-Zavadsky et al. 2020). These M_{dyn}, M_{gas}, and f_{gas} estimates are also listed in Table 4.

Note that we cannot rule out the possibility that the velocity gradient is originally caused by complex dynamics with interacting, merging galaxies. Future higher-resolution observations will confirm the smooth rotation of the disk, or break the complex dynamics down into their multiple components.

4.3. SFR and $L_{[CII]}$ Relation

In the left panel of Figure 8, we show the relation between SFR and $L_{[CII]}$ for $z6.1/6.2$ and $z6.3$. For comparison, we also show local and high-redshift galaxy results taken from the literature (Malhotra et al. 2001; Díaz-Santos et al. 2013; Magdis et al. 2014; De Looze et al. 2014; Herrera-Camus et al. 2015; Spilker et al. 2016; Cooke et al. 2018; Harikane et al. 2020; Matthee et al. 2019; Schaerer et al. 2020) and the $L_{[CII]}$–SFR relation obtained from local star-forming galaxies in De Looze et al. (2014). The observed $L_{[CII]}$ of both $z6.3$ and $z6.1/6.2$ fall within the most luminous $L_{[CII]}$ regime among typical (e.g., SFR $\lesssim 100 \, M_\odot \, yr^{-1}$) high-$z$ star-forming galaxies, demonstrating the power of the gravitational lensing. Following the correction of the lensing magnification, we find that both $z6.3$ and $z6.1/6.2$ fall slightly above, but still follow the

SFR–$L_{[CII]}$ relation of the local galaxies within the dispersion. This is consistent with recent ALMA results, in that the average SFR–$L_{[CII]}$ relation among high-redshift star-forming galaxies at $z \sim 4$–9 is well within the intrinsic dispersion of the local relation (Carniani et al. 2018, 2020; Schaerer et al. 2020). Given that RXCJ0600-z6 is consistent with being an abundant, sub-L^* galaxy at $z = 6$ (see Section 3.5), these results may suggest that the SFR–$L_{[CII]}$ relation, defined by local galaxies, holds from the spatially resolved sub-kpc ISM to the whole scales in abundant galaxies, even up to the epoch of reionization.

To further study the $L_{[CII]}$–SFR relation, the right panel of Figure 8 presents the $L_{[CII]}$/SFR and SFR surface density (ΣSFR). This relation, or another relation between $L_{[CII]}/L_{FIR}$ and L_{FIR} surface density (ΣL_{FIR}), are known to have tight anti-correlations, whereby the deficit of the [C II] line is explained by the high ionization state in the ISM around regions with high ΣSFR or ΣL_{FIR} (e.g., Díaz-Santos et al. 2013; Spilker et al. 2016; Gullberg et al. 2018; Ferrara et al. 2019). Importantly, these relations are not affected by the lensing magnification, because the same magnification factor applies to all these values. We find that $z6.1/6.2$ shows a higher $L_{[CII]}$/SFR ratio, while both $z6.1/6.2$ and $z6.3$ are consistent with the trend of the anti-correlation. This indicates that the difference of ΣSFR causes the difference in the [C II] line luminosity at a given SFR between $z6.1/6.2$ and $z6.3$, which is consistent with the source plane reconstruction results in Section 4.1: the faint [C II]-emitting region of $z6.1/6.2$ is separated from the bright rest-frame UV clumps by $\sim$1.6 kpc in the source plane, where the ionization state of the local ISM is thought to be moderate.

We note that recent ALMA observations show nondetection results for the [C II] line from similarly star-forming galaxies at $z \sim 4$–9 at the same time (see upper limits in Figure 8), which is indicative of the existence of galaxies whose $L_{[CII]}$–SFR relations are different from those of the local galaxies. Given the requirement for prior spectroscopic redshift with the Lyα line in most cases (Section 3.2), these nondetections might be related to recent reports of the potential anti-correlation between $L_{[CII]}$/SFR and EW$_{Ly\alpha}$ (Harikane et al. 2018, 2020; Carniani et al. 2018). In contrast to the most cases, RXCJ0600-z6 is identified in the blind survey, and its physical properties (rest-frame EW$_{Ly\alpha} < 4.4$ Å) agree with the potential anti-correlation reported in Harikane et al. (2018). Another lensed galaxy at $z = 6.15$ (Calura et al. 2021) also follows a similar trend, with relatively large rest-frame EW$_{Ly\alpha}$ (60 ± 8 Å) and small $L_{[CII]}$/SFR ($\sim 2 \times 10^5$). A caveat still remains, in that Schaerer et al. 2020 report a weak dependence of $L_{[CII]}$/SFR on EW$_{Ly\alpha}$. Since the [C II] line emissivity depends on ISM properties, such as the ionization state, metallicity, and gas density (e.g., Vallini et al. 2015), the different $L_{[CII]}$–SFR relations could be alternatively explained by a larger dispersion of the ISM properties in high-z galaxies than in local galaxies. The uncertainties of the SFR estimates might contribute to the large dispersion in high-z galaxies, due to assumptions regarding star formation history, the dust-attenuation curve, and the stellar population age, as discussed in Carniani et al. (2020), and Schaerer et al. (2020). Another recent report regarding the extended [C II] line morphology up to a radius of $\sim$10 kpc (e.g., Fujimoto et al. 2019, 2020b; Ginolfi et al. 2020; Novak et al. 2020) might also be related to some of those nondetections, because the surface brightness of the extended
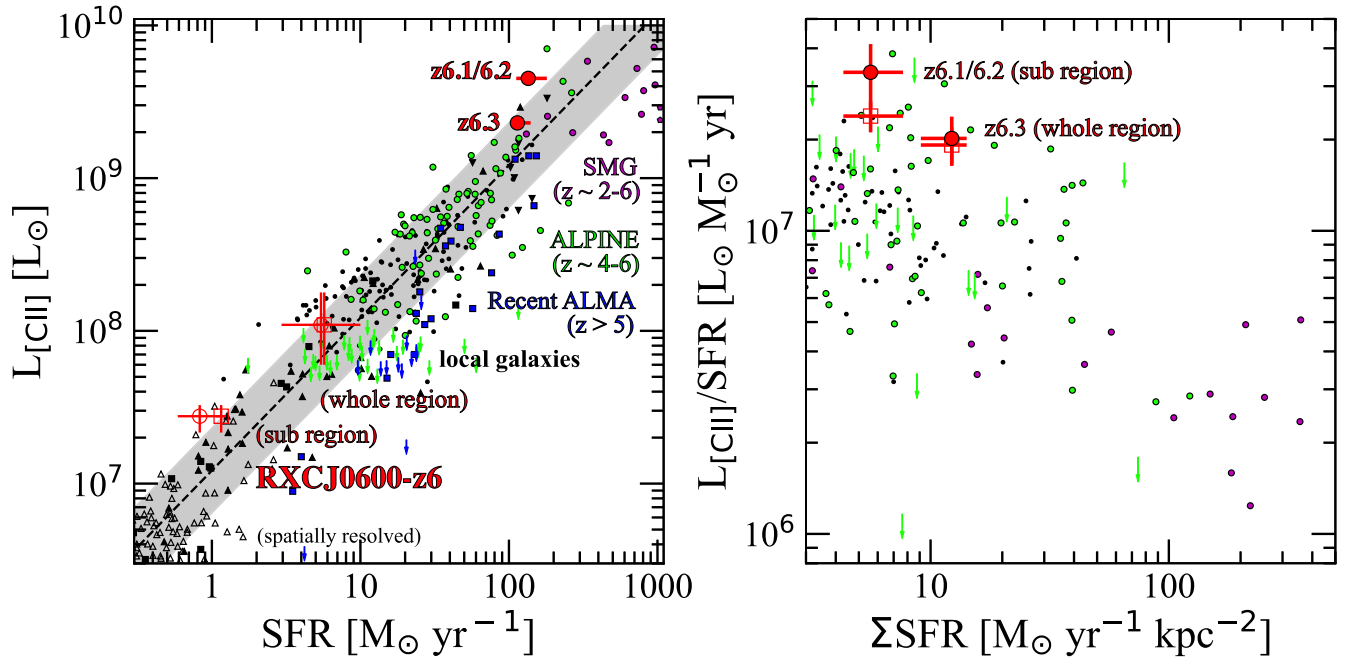
Figure 8. Left: $L_{[CII]}$–SFR relation. The red filled and open circles indicate $z6.1/6.2$ and $z6.3$ before and after the correction of the lensing magnification, respectively. The errors include the uncertainty from the mass models (see Table 3). The red open squares indicate the SFR estimates after the correction of the lensing magnification, based on the conversion from the UV and FIR luminosity of Bell et al. (2005), scaled to the Chabrier IMF. The previous results from local to high-z star-forming galaxies are shown with black circles (local LIRGs; Díaz-Santos et al. 2013), black squares (local dwarfs; De Looze et al. 2014), black triangles (local spirals; Malhotra et al. 2001), black inverse triangles ($z \sim 0.3$ (U)LIRGs; Magdis et al. 2014), green circles ($z \sim 4$–6 star-forming galaxies from ALPINE; Schaerer et al. 2020), magenta pentagons ($z \sim 5$ submillimeter galaxies (SMGs); Cooke et al. 2018), magenta circles ($z \sim 2$–6 lensed SMGs; Spilker et al. 2016), and blue squares (compilation of recent ALMA results for $z > 5$ star-forming galaxies; Matthee et al. 2020 and Harikane et al. 2020). We adopt the average relation of the low-z HII-galaxy/starburst sample from De Looze et al. (2014), which is adjusted to the Chabrier IMF by reducing the SFR by a factor of 1.06, in the same manner as Schaerer et al. (2020). The arrow indicates the 3σ upper limit. The L_{FIR} value in the literature is first converted into a total IR luminosity, L_{TIR} (8–1000 μm), and we then calculate the SFR using the calibration of Murphy et al. (2011). The spatially resolved results (ΣSFR and $\Sigma L_{[CII]}$) for local galaxies are also presented, indicated by open triangles (Herrera-Camus et al. 2015), assuming an area of 1 kpc^2. The dashed line and gray shading denote the $L_{[CII]}$–SFR relation obtained from local star-forming galaxies (De Looze et al. 2014) and its dispersion, respectively. Right: $L_{[CII]}$/SFR–ΣSFR relation. The color assignments on the symbols are the same as those in the left panel. We define the star-forming area as a circular area of the rest-frame UV emission with a radius of $\sqrt{2} \times r_{e,circ}$ for the Σ SFR estimate. We use a factor of $\sqrt{2}$ in accordance with Spilker et al. (2016). For $z6.1/6.2$ and $z6.3$, we evaluate the rest-frame UV size by reducing the [C II] size measurements from IMFIT (Table 1) by a factor of 2 (see Section 4.1). For the ALPINE sources, we use the rest-frame UV size measurement results from Fujimoto et al. (2020b). For local LIRGs and lensed SMGs, we use the rest-frame FIR size measurement results from Spilker et al. (2016), assuming that the star-forming activity dominates in the rest-frame FIR-emitting regions in these objects.

emission is significantly decreased in relatively high-resolution maps (Carniani et al. 2020). Based on visibility-based stacking, the secondary extended component up to the 10 kpc scale is estimated to have an average contribution to the total line luminosity of $\sim$50% around star-forming galaxies (Fujimoto et al. 2019), and $\sim$20% around quasars (Novak et al. 2020) at $z \sim 6$. These non-negligible contributions may be significant if the request sensitivity is close to the detection limit around the 5σ level. However, this is not the case if the carbon in the extended [C II] gas is ionized, by e.g., gravitational energy in the cold stream, shock heating in the outflow and/or inflow gas, or AGN feedback, rather than photoionization powered by the star-forming regions (see e.g., Section 5 of Fujimoto et al. 2019).

4.4. [C II] Luminosity Function

A key goal of ALCS is to constrain the number density of the line emitters. Although the complete blind line survey results with all 33 fields will be presented in a separate paper (in preparation), we can evaluate a lower limit of the [C II] luminosity function at $z \sim 6$ with our [C II] line detection from the strongly lensed LBG at $z = 6.0719$.

To do this, we first measure the effective survey area using mass models for all 33 ALCS clusters at $z \sim 6$, constructed in

the same manner as described in Section 3.3. After the correction of the lensing magnification, we obtain an effective survey area of $\sim$49 (2) arcmin^2 at $L_{[CII]} = 1.0 \times 10^9$ (10^8) $L_\odot$, assuming the line width at FWHM = 200 km s^{-1}, and with a 5σ detection limit. We then convert the effective survey area to the survey volume, based on the frequency setup in the ALCS observations covering the [C II] line emission at $z = 5.974$–6.172 and 6.381–6.602, and derive a lower limit of the [C II] luminosity function at $z = 6$.

In Figure 9, we present the number density of [C II] line emitters at $z = 6$, including recent [C II] line studies at $z > 4$ (Swinbank et al. 2012; Matsuda et al. 2015; Yamaguchi et al. 2017; Cooke et al. 2018; Hayatsu et al. 2019; Decarli et al. 2020; Yan et al. 2020). For comparison, we also present [C II] luminosity functions from semi-analytical models (Popping et al. 2016; Lagache et al. 2018) and from the observed SFR function (SFRF; Smit et al. 2016) of optically-selected galaxies. For the conversion from SFRF to the [C II] luminosity function, we adopt the [C II]–SFR relation of the local star-forming galaxies as estimated in De Looze et al. (2014). We find that our lower limit estimate is consistent with both the semi-analytical results and SFRF. Note that we do not apply any completeness corrections to our lower limit estimate. The incompleteness for strongly lensed sources with large spatial
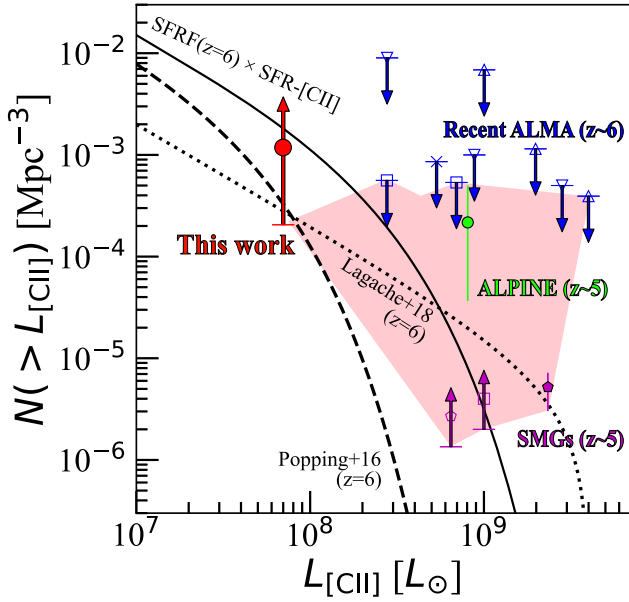
Figure 9. Cumulative [C II] luminosity function at $z = 6$ with recent [C II] line studies at $z > 4$. The red circle shows the number density of the [C II] line emitter, based on our successful detection from the strongly lensed LBG with the effective survey volume of the full ALCS data cubes, composed of 33 galaxy clusters. The lower limit is estimated from the Poisson uncertainty at the single-sided confidence level of 84.13% presented in Gehrels (1986). Recent ALMA blind line survey results are indicated by the blue triangle (243 archival data cubes; Matsuda et al. 2015), blue inverse triangle (four massive galaxy clusters; Yamaguchi et al. 2017), blue square (ASPECS; Decarli et al. 2020), and blue cross (SSA22; Hayatsu et al. 2017, 2019), respectively. The green circle represents the ALPINE results (Yan et al. 2020; Loiacono et al. 2021). Here we show only the estimate from the serendipitous [C II] line detection at $z \sim 5$, whose redshift is sufficiently separated from (i.e., not associated with) the central ALPINE targets. The magenta square and pentagon show the serendipitous [C II] line detection from bright SMGs at $z \sim 5$ reported in Swinbank et al. (2012), and Cooke et al. (2018), respectively. The red shading indicates the current constraints based on both our results and previous results obtained to date. For comparison, we also present the semi-analytical model results (Popping et al. 2016; Lagache et al. 2018) and SFR function (SFRF; Smit et al. 2016), including the dust correction based on the SMC extinction law, whose SFR value is converted into $L_{[CII]}$ with the local [C II]–SFR relation (De Looze et al. 2014).

sizes is generally significant, due to its low surface brightness (e.g., Bouwens et al. 2017; Kawamata et al. 2018; Fujimoto et al. 2017). Although the incompleteness largely depends on the assumption of the intrinsic source size, this may indicate that the lower limit could be placed still higher, and that the faint end of the [C II] luminosity function might be close to SFRF. Indeed, other constraints from the recent [C II] line studies are also consistent with SFRF at the bright regime ($L_{[CII]} \gtrsim 10^{8.5} L_{\odot}$). Although the brightest end ($L_{[CII]} \gtrsim 10^{9.2} L_{\odot}$) of SFRF is smaller than the constraints obtained from the SMG studies (Cooke et al. 2018), this is explained by the absence of such dusty, obscured galaxies in the SFRF, based on the optically-selected galaxies. Therefore, the constraints of the [C II] luminosity function obtained so far are likely to be consistent with the prediction based on the local SFR–$L_{[CII]}$ relation and the SFRF at $z = 6$.

4.5. From ISM to Cosmic Scales

The source plane reconstruction in Section 4.1 reveals the ISM structure down to a scale of a few hundred parsecs, where

we find that the [C II] line is not displaced beyond a $\sim$300 pc from the rest-frame UV continuum, from the spatially resolved ISM to the whole galaxy. In Section 4.3, we find that the SFR–$L_{[CII]}$ relations from the spatially resolved ISM to the whole galaxy are consistent with those of local galaxies. In Section 4.4, we obtain the lower limit at the faintest regime of the $z = 6$ [C II] luminosity function. We find that the prediction from the $z = 6$ SFR function and the SFR–$L_{[CII]}$ relation of the local galaxies is consistent with both our own and previous constraints on the $z = 6$ [C II] luminosity function in the wide $L_{[CII]}$ range. Given the unbiased aspect of the ALCS survey, and indeed the representative physical properties of RXCJ0600-$z6$ among the abundant population of the low-mass regime of $z \sim 6$ star-forming galaxies (Section 3.5), our results may imply that the SFR–$L_{[CII]}$ relation of local star-forming galaxies is universal for a wide range of scales, including the spatially resolved ISM, the whole region of the galaxy, and the cosmic scale.

5. Summary

In this paper, we have presented the blind detection of a multiply imaged line emitter behind the massive galaxy cluster RXCJ0600−2007 in the cycle-6 ALMA large project of the ALMA Lensing Cluster Survey (ALCS). The optical–NIR property, together with our lens model analyses, suggest that the emission line is the [C II] 158 μm line from a Lyman-break galaxy (LBG) at $z = 6.0719 \pm 0.0004$ behind RXCJ0600-2007. We have studied the relation between the star formation rate (SFR) and [C II] line luminosity ($L_{[CII]}$), the morphology, and the kinematics in the spatially resolved interstellar medium (ISM), as well as the whole scale of the LBG, and provided a lower limit at the faint-end of the [C II] luminosity function at $z \sim 6$, with the help of gravitational lensing magnification. The main findings of this paper are summarized as follows:

1. We performed a blind line search for the ALCS data cube in RXCJ0600-2007, and identified two bright lines at $\geqslant 8\sigma$ levels at 268.682 ± 0.011 GHz and 268.744 ± 0.016 GHz, one of which shows a strongly lensed arc shape. Both lines have optical–NIR counterparts with clear Lyman-break feature at $\sim$9000 Å, indicative of the lines corresponding to the [C II] 158 μm at $z = 6.07$. The optical–NIR spectral energy distribution (SED) analysis shows that probability distributions of their photometric redshifts are in excellent agreement with the [C II] line redshift, while other possible FIR lines at $z \sim 6$ struggle to explain the luminosity ratio between the line and the continuum. We therefore conclude that these two lines are [C II] lines.

2. Our lens models, updated with the latest spectroscopic follow-up results with VLT/MUSE, suggest that these lines arise from a strongly magnified and multiply imaged ($\mu \simeq 20-160$) Lyman-break galaxy (LBG) at $z = 6.0719$, with a circularized effective radius of $\sim$0.8 kpc, and an intrinsic luminosity in the rest-frame UV $\sim$3 times fainter ($M_{UV} = -19.7^{+0.5}_{-0.4}$) than the characteristic luminosity at this epoch. A sub-region of the LBG crosses the caustic line in the source plane and is thereby stretched into an arc over $\sim$6″ in the image plane, in which the [C II] line is also significantly detected. Our lens models also predict another two multiple images in this field. We identified the sources at the predicted positions, and found that their

optical–NIR colors agree with the other multiple images of the LBGs. One of these falls within the ALCS area coverage, where we detected a tentative [C II] line (3.0σ) at the same frequency as the other multiple images.

3. After the correction of the lensing magnification, the whole of the LBG and its sub region were characterized with an $L_{[CII]}$ of $1.1^{+0.7}_{-0.5} \times 10^8$ and $0.3^{+0.1}_{-0.1} \times 10^8 \, L_\odot$, an SFR of $5.4^{+4.5}_{-2.9}$ and $0.8^{+0.4}_{-0.2} \, M_\odot \, yr^{-1}$, and a stellar mass ($M_{star}$) of $9.6^{+6.0}_{-4.6} \times 10^8$ and $2.6^{+0.2}_{-1.0} \times 10^8 \, M_\odot$, respectively. From the whole to sub-regions of the LBG, the SFR and M_{star} values fall within the average relation among $z \sim 6$ galaxies, indicating that the LBG is an abundant, representative galaxy at this epoch.

4. The source plane reconstruction resolves the ISM down to $\sim$100–300 pc. The [C II] line from the whole region of the LBG is co-spatial with the rest-frame UV continuum, while the sub region of the LBG is placed $\sim$1.6 kpc away from the galactic center and bright rest-frame UV clumps. The two-peak morphology observed in the [C II] line and rest-frame FIR continuum in the arc show a $\sim$1 kpc offset from the luminosity-weighted center of the sub region of the LBG, which is likely to consists of either a clumpy structure or a smooth disk, but stretched into a two-peak morphology due to perturbation from a foreground galaxy. In these two peaks, the [C II] line and the rest-frame FIR continuum exhibit the *flux ratio anomaly* differently, which suggests that the faint [C II]- and FIR-emitting regions are displaced near the caustic.

5. We find that our results in both whole and sub regions of the LBG fall within the SFR–$L_{[CII]}$ and surface density of SFR (ΣSFR)–$L_{[CII]}$/SFR relations obtained for local star-forming galaxies. The sub-region of the galaxy has a lower ΣSFR and a higher $L_{[CII]}$/SFR value. This is consistent with the absence of the bright rest-frame UV clumps around the sub region of the LBG, located $\sim$1.6 kpc away from the galactic center, where ΣSFR is expected to be low.

6. We find that the LBG is classified as a rotation-dominated system, based on the full observed velocity gradient and the velocity dispersion of the LBG via the bright [C II] line emission. The 3D modeling with ^{3D}BAROLO and GALPAK3D provide consistent results for the rotation kinematics that explain the spatial and velocity offsets of the sub region of the LBG. We estimate the dynamical mass of $M_{dyn} = (3 \pm 1) \times 10^9 \, M_\odot$ and obtain the gas fraction of $\sim$50%–80%.

7. We derive a lower limit on the [C II] luminosity function at $z = 6$, finding that it is consistent with current semi-analytical model predictions. In conjunction with previous ALMA results, we also find that constraints on the [C II] luminosity function at $z = 6$ obtained so far agree with the prediction of the SFR–$L_{[CII]}$ relation of local star-forming galaxies, as well as the SFR function at $z = 6$.

8. With the blind aspect of the ALCS survey and the SFR–$L_{[CII]}$ relations from the sub- to whole regions of the LBG, our results may imply that the local SFR–$L_{[CII]}$ relation is universal for a wide range of scales, including the spatially resolved ISM, the whole region of the galaxy, and the cosmic scale even up to $z = 6$, which we derive in an unbiased manner.

Appendix A
MUSE Spectroscopic Catalog

In Table 5, we summarize the spectroscopic sample from VLT/MUSE (ESO program ID 0100.A-0792, PI: A. Edge) which we use to constrain our lens mass models.

Table 5
MUSE Spectroscopic Catalog

| RELICS ID | R.A. | Decl. | $z_{\rm spec}$ | Flag |
| | deg | deg | | |
(1)	(2)	(3)	(4)	(5)
467	90.0386151	−20.1280873	0.0	4
474	90.0261297	−20.1283111	0.4366	2
490	90.0410860	−20.1282533	0.8943	3
508	90.0352780	−20.1293624	0.0	4
510	90.0366252	−20.1292593	0.4230	3
514	90.0389765	−20.1292234	0.4293	3
524	90.0333696	−20.1293114	0.5614	3
538	90.0258085	−20.1298490	1.0270	9
539	90.0260218	−20.1303021	0.4448	3
543	90.0333594	−20.1313998	0.4299	3
545	90.0346490	−20.1312617	0.4316	3
547	90.0322874	−20.1302526	0.4234	3
571	90.0288919	−20.1307349	0.8751	3
606	90.0317981	−20.1320082	0.2662	3
620	90.0264851	−20.1330304	0.3284	3
624	90.0292841	−20.1331843	0.4164	3
625	90.0286343	−20.1325697	0.3449	3
626	90.0288471	−20.1326848	0.3448	3
647	90.0377894	−20.1333237	0.4176	3
660	90.0400373	−20.1375945	0.3843	3
662	90.0412169	−20.1343049	0.384	3
684	90.0410355	−20.1343563	0.3838	3
685	90.0359084	−20.1336945	0.4190	2
687	90.0328670	−20.1339062	0.2298	3
697	90.0359808	−20.1344771	0.4215	3
699	90.0321831	−20.1357916	0.4245	2
705	90.0332455	−20.1367707	0.0	4
711	90.0349938	−20.1360342	0.4332	3
724	90.0265792	−20.1350258	0.7360	3
735	90.0274334	−20.1354704	0.4280	3
736	90.0257819	−20.1357459	0.4294	3
737	90.0267125	−20.1360004	0.4300	3
742	90.0340260	−20.1357916	0.4266	3
743	90.0376604	−20.1357714	0.4369	3
754	90.0337757	−20.1341905	0.4233	2
772	90.0278737	−20.1374801	0.4307	3
779	90.0326653	−20.1350609	0.4305	3
786	90.0429917	−20.1367709	5.4589	9
791	90.0281193	−20.1381123	0.5089	3
792	90.0335009	−20.1349955	0.4304	3
801	90.0394961	−20.1371561	4.5043	3
802	90.0348279	−20.1356744	0.4319	3
806	90.0364247	−20.1377419	0.4295	3
814	90.0414618	−20.1358813	0.0	4
823	90.0317133	−20.1382886	0.4276	3
836	90.0264868	−20.1381907	0.0	4
860	90.0365781	−20.1393201	0.4177	3
862	90.0279194	−20.1393703	0.4321	3
863	90.0278743	−20.1397608	0.4296	3
870	90.0430009	−20.1395918	0.4392	3
871	90.0425305	−20.1399135	0.3825	3
886	90.0419909	−20.1399491	0.4462	2
887	90.0340961	−20.1398346	0.4315	3
899	90.0295615	−20.1407949	0.4317	3
900	90.0296018	−20.1404579	0.4323	3
938	90.0430509	−20.1413250	0.4197	3
941	90.0343581	−20.1391201	0.4195	3
956	90.0355945	−20.1419747	0.4240	2
957	90.0387747	−20.1421929	0.4314	3
962	90.0306151	−20.1429810	0.0866	3
963	90.0303906	−20.1430867	0.0866	3
964	90.0304180	−20.1428506	0.0866	3

Table 5
(Continued)

| RELICS ID | R.A. | Decl. | $z_{\rm spec}$ | Flag |
| | deg | deg | | |
(1)	(2)	(3)	(4)	(5)
965	90.0304371	−20.1427616	0.0866	3
966	90.0299297	−20.1421244	0.0866	3
967	90.0300655	−20.1424500	0.0866	3
973	90.0349638	−20.1425005	0.4255	3
974	90.0350788	−20.1429515	0.4313	3
990	90.0258089	−20.1429104	0.5491	3
1000	90.0296362	−20.1430670	0.4305	3
1003	90.0384290	−20.1430473	0.5479	9
1024	90.0337998	−20.1436577	2.7722	3
1025	90.0340880	−20.1437083	2.7723	3
1027	90.0351249	−20.1438250	2.7723	9
1029	90.0356487	−20.1438539	2.7725	3
900001	90.0424970	−20.1364998	3.5238	3
900003	90.0283847	−20.1376962	5.4067	9

Note. (1) ID from the RELICS public catalog of hlsp_relics_hst_wf-c3ir_rxc0600-20_multi_v1_cat.txt (https://relics.stsci.edu/). IDs starting with 900 are MUSE detections, with no counterpart in the aforementioned catalog. (2) Observed R.A. in degrees. (3) Observed decl. in degrees. (4) MUSE spectroscopic redshift. (5) Redshift quality flag. 2: likely, 3: secure measurement, 9: single line measurement, and 4: field stars.

Appendix B
Two-peak Morphology in $z6.1/6.2$

To check the possibility that the two-peak morphology of the [C II] line in $z6.1/6.2$ is caused by noise fluctuation, boosted by the underlying diffuse emission (e.g., Hodge et al. 2016), we perform a mock observation using the CASA SIMOBSERVE software toward $z6.1/6.2$, in the same manner as Fujimoto et al. (2020a). Here we assume the single elliptical Gaussian for the [C II] line surface brightness distribution of $z6.1/6.2$, based on the IMFIT results in the uv-tapered map (Section 3.1). We then obtain the visibility data set via SIMOBSERVE, and produce the natural-weighted velocity-integrated map of the [C II] line. We repeat the mock observation 1000 times to produce the map. Given a spatial offset of $\sim 2''0$, and significance levels of 8.2σ and 5.4σ between the two peaks in $z6.1/6.2$, we then search multiple positive peaks that are located with spatial offsets of less than $2''5$, and detected at $\geqslant 5.4\sigma$ levels, utilizing SExtractor version 2.5.0 (Bertin & Arnouts 1996). We identify 7 out of 1000 maps with multiple peaks that meet the above criteria. These results indicate that the two-peak morphology of the [C II] line in $z6.1/6.2$ might be caused by noise fluctuation, with a probability of $\sim 0.7\%$. Note that we find that all multiple peaks identified in the 7 maps show their flux ratios to be almost identical, which is different from the two peaks observed in $z6.1/6.2$ (ratio $\sim 8:5$). This indicates that the close separation, as well as the flux ratio of the two peaks observed in $z6.1/6.2$, is insufficiently explained in terms of noise fluctuation. In fact, we identify only 1 out of 1000 maps with a flux ratio of multiple peaks similar to the two peaks in $z6.1/6.2$, but with a spatial offset of $4''7$. Therefore, we conclude that the possibility of noise fluctuation is negligible in the two-peak [C II] line morphology of $z6.1/6.2$.

Appendix C
Optical–NIR Photometry

We adopt separate strategies for extracting robust photometry for the four lensed images, as described below, to account for the crowded cluster field and varying degrees of extended source morphology. In general, we model the full IRAC mosaics using a strategy similar to that of Merlin et al. (2015), where we use image thumbnails of each source and neighbors taken from the high-resolution HST/WFC3 F160W image, together with knowledge of the WFC3 and IRAC point-spread functions (PSFs), to model the low-resolution IRAC image.

C.1. Images z6.3 and z6.5

The sources of interest in these images are relatively bright and fairly well separated from their nearest bright (projected) neighbors (Figure 1). We measure aperture flux densities in each of the HST filters, using fixed $D = 0\rlap.{''}7$ apertures centered on the source of interest to define the colors. To determine the overall flux normalization, we model the source morphology of the lensed image and nearby neighbors, using the nonparametric morphological fitting code SCARLET (Melchior et al. 2018). All of the WFC3/IR images (and their PSFs) are used to constrain the SCARLET morphological model. We scale all of the HST aperture measurements $F_{ap,i}$ by the aperture correction $F_{S,F160W}/F_{ap,F160W}$, where $F_{S,F160W}$ is the integral of the SCARLET model evaluated in the F160W filter, and $F_{S,F160W}$ is the aperture measurement in that filter. The photometric uncertainties are measured in the same apertures on the inverse variance image in each filter. For the IRAC flux densities of these images, we subtract all modeled sources other than the source of interest, and perform aperture photometry on this cleaned image using $D = 3\rlap.{''}0$ apertures, which we correct to the same "total" scale as for HST, using aperture corrections of 1.6 and 1.7 for channels 1 and 2, respectively, derived from a separate bright, isolated source in the field.

C.2. Extended Arc Image z6.1/6.2

This image is a highly elongated arc extending over ≈ 6 arcsec coincident, with a foreground compact source in the center (Figure 1). Here, we model both overlapping sources in the F160W image as parametric Sérsic profiles, using GALFIT software (Peng et al. 2010). For the photometry of the lensed arc and foreground image in the WFC3/IR filters, we fit for the relative normalizations of the two Sérsic components convolved with the appropriate PSFs. For IRAC, we convolve the model Sérsic profiles with the IRAC PSF and fit for the normalization of the source of interest and all neighboring sources via least-squares optimization. As for HST, the normalization of the scaled morphological components is adopted as the photometric measurement without additional aperture corrections. For the optical images where the arc is not readily visible, we measure an aperture flux density and its associated uncertainty within a large rectangle aperture of approximately $1\rlap.{''}2 \times 3\rlap.{''}0$.

Note that the deblended color of the foreground object is similar to the color of cluster members, and the best-fit SED shows the photometric redshift at $0.57^{+0.14}_{-0.17}$, which is close to the cluster redshift at $z = 0.43$ (see also Laporte et al. 2021). Although this suggests the foreground to be one of the cluster

members, we do not include it in our fiducial mass model due to potential systematics in the de-blending process. A detailed examination of the contribution of the foreground object to morphology and magnification factors of $z6.1/6.2$ (Section 4.1) must be investigated after we obtain the spectroscopic redshift of the foreground object.

C.3. Faint Image z6.4

The final faint image of $z6.4$ is close to the cluster core and the BCG. Although it is not deblended as a separate source in our original photometric catalog (and associated IRAC model), a source is readily apparent in the F160W image (Figure 1). We estimate the photometry of this image by placing fixed $D = 0\rlap.{''}7$ and $D = 3\rlap.{''}0$ apertures, centered on the F160W position in the HST and IRAC filter mosaics, respectively, and scale these measurements by the aperture corrections derived for the point sources.

Appendix D
[C II] Spectra of z6.1 and z6.2

As a sanity check of our interpretation that one of the [C II] line emitters consists of a pair of multiple images of $z6.1$ and $z6.2$, we compare the [C II] spectra of $z6.1$ and $z6.2$. In Figure 10, we show the [C II] spectra of $z6.1$ (red line) and $z6.2$ (blue line), normalized to the peak of $z6.1/6.2$ (black line). We find that $z6.1$ and $z6.2$ have [C II] line profiles consistent with each other within the errors, which agrees with our interpretation of $z6.1$ and $z6.2$ being a pair of multiple images.
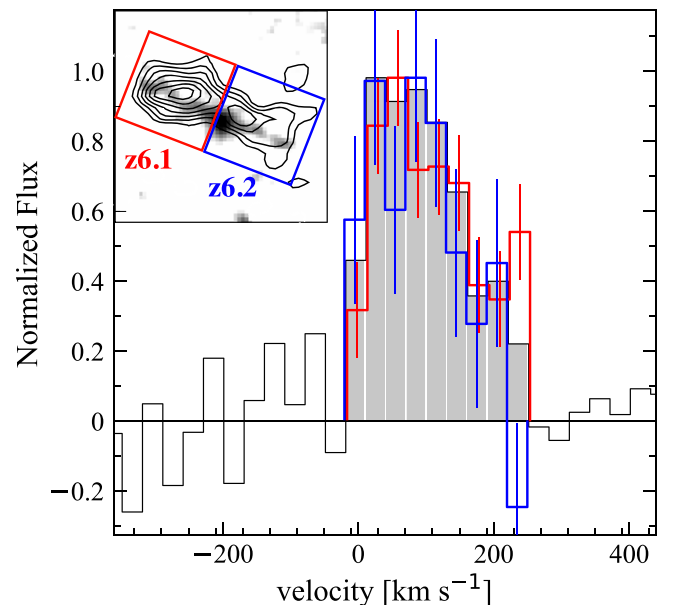

Figure 10. Zoomed-in [C II] line spectra of $z6.1$ and $z6.2$ as a function of velocity with respect to the frequency peak of $z6.3$. The inset panel shows the same image cutout as the middle panel of Figure 1 for $z6.1/6.2$. The red and blue squares denote apertures that are used to produce the [C II] spectra for $z6.1$ and $z6.2$, respectively. The black line and the gray shade indicate the integrated [C II] line spectrum of $z6.1/6.2$ and the [C II]-detected channels, respectively. The red and blue lines present the [C II] spectra for $z6.1$ and $z6.2$, respectively, normalized to the peak of the integrated spectrum.

Table 6
3D Modeling Results

| | 3D BAROLO | | | GALPAK3D |
	Ring1	Ring2	Ring3	Exponential disk
radius[a] (9″)	0–0.45	0.45–0.9	0.9–1.35	0.55 ± 0.02
v_{LOS}[b] (km s^{-1})	22^{+5}_{-4}	76^{+22}_{-22}	62^{+4}_{-3}	62 ± 4
σ_{vel} (km s^{-1})	46^{+9}_{-8}	54^{+11}_{-11}	59^{+7}_{-7}	55 ± 3
incl. (deg)	56	57	59	57 ± 3
PA[c] (°)	36	32	27	21 ± 3

Notes.
[a] Inner and outer radii of the tilted rings for 3D BAROLO and effective radius for GALPAK3D. The turnover radius is estimated to be $0''62 \pm 0''11$ in the tanh formalization for the rotation curve in GALPAK3D.
[b] Line-of-sight projected rotation velocity. We present V_{max} for GALPAK3D.
[c] We follow the definition of PA as the orientation from the y-axis in anti-clockwise, which is different to that of the original output of 3D BAROLO.

Appendix E
[C II] Rotation Modeling

In Section 4.2, we find that z6.3 is likely a rotation-dominated system. In Table 6, we summarize the 3D modeling results for the [C II] line around z6.3 from 3D BAROLO (Di Teodoro & Fraternali 2015) and GALPAK3D (Bouché et al. 2015). For 3D BAROLO, since the ALMA beam has a half-width-at-half-maximum (HWHM) of ~$0''45$ at the [C II] line frequency along the orientation of the velocity gradient, we adopt three (~1.4/0.45) annuli with widths of $0''45$ for the tilted ring fitting algorithm. We use the THRESHOLD mask with a 2σ limit for the data cube, and the spatial center, systemic velocity, rotation velocity (v_{rot}), velocity dispersion (σ_{vel}), position angle (PA), and inclination (incl.) are used as free parameters in the fitting. The errors are estimated based on the minimization algorithm in a Monte Carlo approach. For GALPAK3D, we adopt the exponential disk for the flux profile, the Gaussian for the thickness profile, and the tanh formalization of $V_{max} \times \tanh(r/r_V)$ for the rotation curve, where V_{max} and r_V are the maximum velocity and the turnover radius, respectively. In place of the mask, we use a cutout data cube of $3''8 \times 3''8$ and $[-120: +120]$ km s^{-1} for the fitting. We set a maximum iteration number of 20,000. The spatial center, systemic velocity, flux, r_e, PA, incl., r_V, V_{max}, and σ_{vel} are used as free parameters. The errors are evaluated based on a Markov chain Monte Carlo approach.

ORCID iDs

Seiji Fujimoto ⓘ https://orcid.org/0000-0001-7201-5066
Masamune Oguri ⓘ https://orcid.org/0000-0003-3484-399X
Gabriel Brammer ⓘ https://orcid.org/0000-0003-2680-005X
Yuki Yoshimura ⓘ https://orcid.org/0000-0002-1413-1963
Nicolas Laporte ⓘ https://orcid.org/0000-0001-7459-6335
Kotaro Kohno ⓘ https://orcid.org/0000-0002-4052-2394
Adi Zitrin ⓘ https://orcid.org/0000-0002-0350-4488
Johan Richard ⓘ https://orcid.org/0000-0001-5492-1049
Franz E. Bauer ⓘ https://orcid.org/0000-0002-8686-8737
Ian Smail ⓘ https://orcid.org/0000-0003-3037-257X
Bunyo Hatsukade ⓘ https://orcid.org/0000-0001-6469-8725
Yoshiaki Ono ⓘ https://orcid.org/0000-0001-9011-7605
Vasily Kokorev ⓘ https://orcid.org/0000-0002-5588-9156
Hideki Umehata ⓘ https://orcid.org/0000-0003-1937-0573
Daniel Schaerer ⓘ https://orcid.org/0000-0001-7144-7182
Kirsten Knudsen ⓘ https://orcid.org/0000-0002-7821-8873
Georgios Magdis ⓘ https://orcid.org/0000-0002-4872-2294
Francesco Valentino ⓘ https://orcid.org/0000-0001-6477-4011
Yiping Ao ⓘ https://orcid.org/0000-0003-3139-2724
Sune Toft ⓘ https://orcid.org/0000-0003-3631-7176
Miroslava Dessauges-Zavadsky ⓘ https://orcid.org/0000-0003-0348-2917
Kazuhiro Shimasaku ⓘ https://orcid.org/0000-0002-2597-2231
Karina Caputi ⓘ https://orcid.org/0000-0001-8183-1460
Haruka Kusakabe ⓘ https://orcid.org/0000-0002-3801-434X
Kana Morokuma-Matsui ⓘ https://orcid.org/0000-0003-3932-0952
Minju M. Lee ⓘ https://orcid.org/0000-0002-2419-3068
Timothy Rawle ⓘ https://orcid.org/0000-0002-7028-5588
Daniel Espada ⓘ https://orcid.org/0000-0002-8726-7685

References

Aravena, M., Decarli, R., Walter, F., et al. 2016, ApJ, 833, 71
Bacon, R., Piqueras, L., Conseil, S., Richard, J., & Shepherd, M. 2016, MPDAF: MUSE Python Data Analysis Framework
Bakx, T. J. L. C., Tamura, Y., Hashimoto, T., et al. 2020, MNRAS, 493, 4294
Bell, E. F., Papovich, C., Wolf, C., et al. 2005, ApJ, 625, 23
Bertin, E., & Arnouts, S. 1996, A&A, 117, 393
Béthermin, M., Fudamoto, Y., Ginolfi, M., et al. 2020, A&A, 643, A2
Bouché, N., Carfantan, H., Schroetter, I., Michel-Dansac, L., & Contini, T. 2015, AJ, 150, 92
Bouwens, R. J., van Dokkum, P. G., Illingworth, G. D., et al. 2017, arXiv:1711.02090
Bowler, R. A. A., Bourne, N., Dunlop, J. S., McLure, R. J., & McLeod, D. J. 2018, MNRAS, 481, 1631
Brammer, G. B., van Dokkum, P. G., & Coppi, P. 2008, ApJ, 686, 1503
Brauher, J. R., Dale, D. A., & Helou, G. 2008, ApJS, 178, 280
Calura, F., Vanzella, E., Carniani, S., et al. 2021, MNRAS, 500, 3083
Calzetti, D., Armus, L., Bohlin, R. C., et al. 2000, ApJ, 533, 682
Caminha, G. B., Grillo, C., Rosati, P., et al. 2017, A&A, 607, A93
Caminha, G. B., Rosati, P., Grillo, C., et al. 2019, A&A, 632, A36
Carniani, S., Ferrara, A., Maiolino, R., et al. 2020, MNRAS, 499, 5136
Carniani, S., Gallerani, S., Vallini, L., et al. 2019, MNRAS, 489, 3939
Carniani, S., Maiolino, R., Amorin, R., et al. 2018, MNRAS, 478, 1170
Chabrier, G. 2003, PASP, 115, 763
Chambers, K. C., Magnier, E. A., Metcalfe, N., et al. 2016, arXiv:1612.05560
Chapin, E. L., Pope, A., Scott, D., et al. 2009, MNRAS, 398, 1793
Coe, D., Salmon, B., Bradač, M., et al. 2019, ApJ, 884, 85
Conroy, C., & Gunn, J. E. 2010, ApJ, 712, 833
Conroy, C., Gunn, J. E., & White, M. 2009, ApJ, 699, 486
Cooke, E. A., Smail, I., Swinbank, A. M., et al. 2018, ApJ, 861, 100
De Barros, S., Pentericci, L., Vanzella, E., et al. 2017, A&A, 608, A123
De Looze, I., Cormier, D., Lebouteiller, V., et al. 2014, A&A, 568, A62
Decarli, R., Aravena, M., Boogaard, L., et al. 2020, ApJ, 902, 110
Dessauges-Zavadsky, M., Ginolfi, M., Pozzi, F., et al. 2020, A&A, 643, A5
Dessauges-Zavadsky, M., Richard, J., Combes, F., et al. 2019, NatAs, 3, 1115
Dessauges-Zavadsky, M., Zamojski, M., Rujopakarn, W., et al. 2017, A&A, 605, A81
Di Teodoro, E. M., & Fraternali, F. 2015, MNRAS, 451, 3021
Díaz-Santos, T., Armus, L., Charmandaris, V., et al. 2013, ApJ, 774, 68
Dye, S., Furlanetto, C., Swinbank, A. M., et al. 2015, MNRAS, 452, 2258
Ebeling, H., Edge, A. C., & Henry, J. P. 2001, ApJ, 553, 668
Faisst, A. L., Fudamoto, Y., Oesch, P. A., et al. 2020, MNRAS, 498, 4192
Ferrara, A., Vallini, L., Pallottini, A., et al. 2019, MNRAS, 489, 1
Finkelstein, S. L., Papovich, C., Dickinson, M., et al. 2013, Natur, 502, 524
Flewelling, H. A., Magnier, E. A., Chambers, K. C., et al. 2020, ApJS, 251, 7
Förster Schreiber, N. M., Genzel, R., Bouché, N., et al. 2009, ApJ, 706, 1364
Fujimoto, S., Oguri, M., Nagao, T., Izumi, T., & Ouchi, M. 2020a, ApJ, 891, 64
Fujimoto, S., Ouchi, M., Ferrara, A., et al. 2019, ApJ, 887, 107
Fujimoto, S., Ouchi, M., Shibuya, T., & Nagai, H. 2017, ApJ, 850, 83
Fujimoto, S., Silverman, J. D., Bethermin, M., et al. 2020b, ApJ, 900, 1
Gaia Collaboration, Brown, A. G. A., Vallenari, A., et al. 2018, A&A, 616, A1
Gallerani, S., Pallottini, A., Feruglio, C., et al. 2018, MNRAS, 473, 1909

Gehrels, N. 1986, ApJ, 303, 336
Ginolfi, M., Jones, G. C., Béthermin, M., et al. 2020, A&A, 633, A90
González-López, J., Bauer, F. E., Aravena, M., et al. 2017, A&A, 608, A138
Goodman, A. A., Rosolowsky, E. W., Borkin, M. A., et al. 2009, Natur, 457, 63
Gullberg, B., Swinbank, A. M., Smail, I., et al. 2018, ApJ, 859, 12
Harikane, Y., Ouchi, M., Inoue, A. K., et al. 2020, ApJ, 896, 93
Harikane, Y., Ouchi, M., Shibuya, T., et al. 2018, ApJ, 859, 84
Hashimoto, T., Inoue, A. K., Mawatari, K., et al. 2019, PASJ, 71, 71
Hashimoto, T., Laporte, N., Mawatari, K., et al. 2018, Natur, 557, 392
Hatsukade, B., Tamura, Y., Iono, D., et al. 2015, PASJ, 67, 93
Hayatsu, N. H., Ivison, R. J., Andreani, P., et al. 2019, RNAAS, 3, 97
Hayatsu, N. H., Matsuda, Y., Umehata, H., et al. 2017, PASJ, 69, 45
Herrera-Camus, R., Bolatto, A. D., Wolfire, M. G., et al. 2015, ApJ, 800, 1
Higuchi, R., Ouchi, M., Ono, Y., et al. 2019, ApJ, 879, 28
Hodge, J. A., Swinbank, A. M., Simpson, J. M., et al. 2016, ApJ, 833, 103
Holwerda, B. W., Bouwens, R., Oesch, P., et al. 2015, ApJ, 808, 6
Inoue, A. K., Tamura, Y., Matsuo, H., et al. 2016, Sci, 352, 1559
Iye, M., Ota, K., Kashikawa, N., et al. 2006, Natur, 443, 186
Iyer, K., Gawiser, E., Davé, R., et al. 2018, ApJ, 866, 120
Jones, G. C., Carilli, C. L., Shao, Y., et al. 2017, ApJ, 850, 180
Jullo, E., Kneib, J. P., Limousin, M., et al. 2007, NJPh, 9, 447
Kawamata, R., Ishigaki, M., Shimasaku, K., et al. 2018, ApJ, 855, 4
Kawamata, R., Oguri, M., Ishigaki, M., Shimasaku, K., & Ouchi, M. 2016, ApJ, 819, 114
Knudsen, K. K., Richard, J., Kneib, J.-P., et al. 2016, MNRAS, 462, L6
Kohandel, M., Pallottini, A., Ferrara, A., et al. 2019, MNRAS, 487, 3007
Kriek, M., & Conroy, C. 2013, ApJL, 775, L16
Kusakabe, H., Blaizot, J., Garel, T., et al. 2020, A&A, 638, A12
Lagache, G., Cousin, M., & Chatzikos, M. 2018, A&A, 609, A130
Laporte, N., Katz, H., Ellis, R. S., et al. 2019, MNRAS, 487, L81
Laporte, N, Zitrin, A, Ellis, R S, et al. 2021, MNRAS, (in press)
Le Fèvre, O., Béthermin, M., Faisst, A., et al. 2020, A&A, 643, A1
Loiacono, F., Decarli, R., Gruppioni, C., et al. 2021, A&A, 646, A76
Lotz, J. M., Koekemoer, A., Coe, D., et al. 2017, ApJ, 837, 97
Magdis, G. E., Rigopoulou, D., Hopwood, R., et al. 2014, ApJ, 796, 63
Maiolino, R., Carniani, S., Fontana, A., et al. 2015, MNRAS, 452, 54
Maiolino, R., & Mannucci, F. 2019, A&ARv, 27, 3
Malhotra, S., Kaufman, M. J., Hollenbach, D., et al. 2001, ApJ, 561, 766
Mao, S., & Schneider, P. 1998, MNRAS, 295, 587
Matsuda, Y., Nagao, T., Iono, D., et al. 2015, MNRAS, 451, 1141
Matthee, J., Sobral, D., Boogaard, L. A., et al. 2019, ApJ, 881, 124
Matthee, J., Sobral, D., Boone, F., et al. 2017, ApJ, 851, 145
Matthee, J., Sobral, D., Gronke, M., et al. 2020, MNRAS, 492, 1778
McMullin, J. P., Waters, B., Schiebel, D., Young, W., & Golap, K. 2007, in ASP Conf. Ser., 376, Astronomical Data Analysis Software and Systems XVI, ed. R. A. Shaw, F. Hill, & D. J. Bell (San Francisco, CA: ASP), 127
Melchior, P., Moolekamp, F., Jerdee, M., et al. 2018, A&C, 24, 129
Merlin, E., Fontana, A., Ferguson, H. C., et al. 2015, A&A, 582, A15
Murphy, E. J., Condon, J. J., Schinnerer, E., et al. 2011, ApJ, 737, 67
Navarro, J. F., Frenk, C. S., & White, S. D. M. 1997, ApJ, 490, 493
Novak, M., Bañados, E., Decarli, R., et al. 2019, ApJ, 881, 63
Novak, M., Venemans, B. P., Walter, F., et al. 2020, ApJ, 904, 131
Oesch, P. A., Brammer, G., van Dokkum, P. G., et al. 2016, ApJ, 819, 129
Oesch, P. A., van Dokkum, P. G., Illingworth, G. D., et al. 2015, ApJL, 804, L30

Oguri, M. 2010, PASJ, 62, 1017
Oke, J. B., & Gunn, J. E. 1983, ApJ, 266, 713
Ono, Y., Ouchi, M., Harikane, Y., et al. 2018, PASJ, 70, S10
Ono, Y., Ouchi, M., Mobasher, B., et al. 2012, ApJ, 744, 83
Pavesi, R., Riechers, D. A., Capak, P. L., et al. 2016, ApJ, 832, 151
Peng, C. Y., Ho, L. C., Impey, C. D., & Rix, H.-W. 2010, AJ, 139, 2097
Pentericci, L., Carniani, S., Castellano, M., et al. 2016, ApJL, 829, L11
Pentericci, L., Fontana, A., Vanzella, E., et al. 2011, ApJ, 743, 132
Pentericci, L., Vanzella, E., Castellano, M., et al. 2018, A&A, 619, A147
Pentericci, L., Vanzella, E., Fontana, A., et al. 2014, ApJ, 793, 113
Piqueras, L., Conseil, S., Shepherd, M., et al. 2017, arXiv:1710.03554
Planck Collaboration, Abergel, A., Ade, P. A. R., et al. 2011, A&A, 536, A21
Popping, G., van Kampen, E., Decarli, R., et al. 2016, MNRAS, 461, 93
Postman, M., Coe, D., Benítez, N., et al. 2012, ApJS, 199, 25
Rizzo, F., Vegetti, S., Powell, D., et al. 2020, Natur, 584, 201
Roberts-Borsani, G. W., Bouwens, R. J., Oesch, P. A., et al. 2016, ApJ, 823, 143
Romano, M., Cassata, P., Morselli, L., et al. 2020, MNRAS, 496, 875
Rybak, M., Hodge, J. A., Vegetti, S., et al. 2020, MNRAS, 494, 5542
Rybak, M., McKean, J. P., Vegetti, S., Andreani, P., & White, S. D. M. 2015, MNRAS, 451, L40
Schaerer, D., Ginolfi, M., Bethermin, M., et al. 2020, A&A, 643, A3
Shibuya, T., Kashikawa, N., Ota, K., et al. 2012, ApJ, 752, 114
Shibuya, T., Ouchi, M., & Harikane, Y. 2015, ApJS, 219, 15
Shibuya, T., Ouchi, M., Harikane, Y., et al. 2018, PASJ, 70, S15
Smit, R., Bouwens, R. J., Carniani, S., et al. 2018, Natur, 553, 178
Smit, R., Bouwens, R. J., Labbé, I., et al. 2016, ApJ, 833, 254
Soto, K. T., Lilly, S. J., Bacon, R., Richard, J., & Conseil, S. 2016, MNRAS, 458, 3210
Spilker, J. S., Aravena, M., Béthermin, M., et al. 2018, Sci, 361, 1016
Spilker, J. S., Marrone, D. P., Aravena, M., et al. 2016, ApJ, 826, 112
Stark, D. P., Ellis, R. S., Charlot, S., et al. 2017, MNRAS, 464, 469
Stark, D. P., Ellis, R. S., & Ouchi, M. 2011, ApJL, 728, L2
Strait, V., Bradač, M., Coe, D., et al. 2020, ApJ, 888, 124
Swinbank, A. M., Karim, A., Smail, I., et al. 2012, MNRAS, 427, 1066
Swinbank, A. M., Smail, I., Longmore, S., et al. 2010, Natur, 464, 733
Swinbank, A. M., Vernet, J. D. R., Smail, I., et al. 2015, MNRAS, 449, 1298
Tamura, Y., Mawatari, K., Hashimoto, T., et al. 2019, ApJ, 874, 27
Tamura, Y., Oguri, M., Iono, D., et al. 2015, PASJ, 67, 72
Tilvi, V., Papovich, C., Finkelstein, S. L., et al. 2014, ApJ, 794, 5
Treu, T., Schmidt, K. B., Trenti, M., Bradley, L. D., & Stiavelli, M. 2013, ApJL, 775, L29
Vallini, L., Gallerani, S., Ferrara, A., Pallottini, A., & Yue, B. 2015, ApJ, 813, 36
Vanzella, E., Meneghetti, M., Caminha, G. B., et al. 2020, MNRAS, 494, L81
Vanzella, E., Pentericci, L., Fontana, A., et al. 2011, ApJL, 730, L35
Weilbacher, P. M., Streicher, O., Urrutia, T., et al. 2014, in ASP Conf. Ser., 485, Astronomical Data Analysis Software and Systems XXIII, ed. N. Manset & P. Forshay (San Francisco, CA: ASP), 451
Williams, J. P., de Geus, E. J., & Blitz, L. 1994, ApJ, 428, 693
Yamaguchi, Y., Kohno, K., Tamura, Y., et al. 2017, ApJ, 845, 108
Yan, L., Sajina, A., Loiacono, F., et al. 2020, ApJ, 905, 147
Zanella, A., Daddi, E., Magdis, G., et al. 2018, MNRAS, 481, 1976
Zitrin, A., Fabris, A., Merten, J., et al. 2015, ApJ, 801, 44